2018

Computations of the Dynamic Fracture of Plane Structures by the Extended Finite Element Method

Iman Asareh
University of South Carolina

Computations of the Dynamic Fracture of Plane Structures by the Extended Finite Element Method

by

Iman Asareh

Bachelor of Science
Shahid Chamran University of Ahvaz, 2007

Master of Science
Sharif University of Technology, 2010

Submitted in Partial Fulfillment of the Requirements

for the Degree of Doctor of Philosophy in

Civil Engineering

College of Engineering and Computing

University of South Carolina

2018

Accepted by:

Robert Mullen, Major Professor

Juan Caicedo, Committee Member

Fabio Matta, Committee Member

Xiaomin Deng, Committee Member

Cheryl L. Addy, Vice Provost and Dean of the Graduate School

Dedication

To my Parents, Ozra and Mohammad Kazem and my dear fiancé Narges.

Acknowledgments

First, I would like to express thanks to my former advisor, Dr. Jeong-Hoon Song. Dr. Song was certainly a tremendous mentor for me. He supported my research for several years and sincerely encouraged me to grow as a research scientist. I also would like to express my sincerest gratitude to Professor Robert Mullen for his support and guidance throughout my graduate studies.

I also would like to express the gratitude to my Master advisor Professor Alireza Khaloo, who sincerely guided me to attend the Ph.D. program at University of South Carolina. I also would like to thank Professor Mohsen Ghaemian and Professor Hamid Reza Ghafouri for their helpful guidance.

I was fortunate to have accomplished faculties as committee members, Dr. Juan Caicedo, Dr. Fabio Matta and Dr. Xiaomin Deng. I am indebted to them for their effort to review this work and for their helpful comments.

I also appreciate the support of my family, friends and colleagues in my research group for their valuable support. Finally, I would like to express a great deal of sincere gratitude to my dear fiancé, Dr. Narges Kaveshgar who has always been a great inspiration to me with her endless encouragement.

Abstract

Finite element methods for the simulation of dynamic fracture in plane structures are presented. The method is a modified extended finite element method (XFEM) for dynamic fracture simulations with a new methodology to construct the XFEM basis functions for discontinuities. In contrast to conventional XFEM in which the extended interpolation is defined to only capture the discontinuities, the proposed method describes the enrichment functions so that they reproduce both the discontinuities and the polynomial bases of sufficiently high order which are critical for finite element convergence. Such enrichment functions, by adopting the Duffy's transformation, can be simply defined in terms of standard shape functions. The approach is applied to a linear three-node triangular element for element-by-element crack propagation modeling.

In the proposed method, the enrichment parameters effectively represent the physics of the discontinuity and are assigned to non-nodal points, which helps to simply impose Dirichlet boundary conditions in strong form. This feature successfully dissociates the finite element nodes from the extended approximation; it facilitates the treatment of arbitrary crack propagation in explicit methods.

The proposed method significantly simplifies the XFEM programming implementation; the enrichment functions are vanished outside the element domain without shifting techniques, so that no blending of the local partition unity is required. In addition, the enriching procedure depends on neither the crack direction nor the elements contiguous to the enriched element. Moreover, the proposed method facilitates the treatment of crack modeling in object-oriented programs (OOP) as the enrich-

ment object is completely dissociated from the element nodes.

The proposed method combined with explicit time integration and a cohesive law quite well simulates the dynamic fracture of ductile and brittle materials. The methodology is applied to the simulation of several benchmark problems whose experimental results are available involving dynamic fracture and nonlinearities. The numerical results in terms of crack paths and speeds were effectively computed and matched the experimental results. The results are also compared to those obtained by standard XFEM to demonstrate the efficacy of the method. Through these numerical examples, the robustness and performance of the method in reproducing the observed failure modes are demonstrated.

Table of Contents

List of Tables

List of Figures

Introduction

The extended finite element method (XFEM) [7, 25] can be viewed as a variation of the generalized finite element method (GFEM) introduced by Melenk and Babuška [2] whereby arbitrary discontinuities such as crack and shear band can be modeled without remeshing. One advantage of the XFEM over the GFEM is that it permits the use of local enrichment bases in the finite element (FE) approximation. For the FE convergence, completeness is a necessary condition [23, 9], i.e. the local approximation must be capable of reproducing given smooth functions, which for elasticity are rigid body motions and constant strain states. However, the local approximation in conventional XFEM focuses only on reproducing the discontinuous functions along with meeting of compatibility conditions among enriched element and its contiguous elements. Therefore, in many instances, it is not apparent how to be the XFEM convergence rates with mesh refinement.

The XFEM exploits the partition of unity framework to adopt various functions as a basis for reproducing the discontinuous fields; step enrichment functions for strong discontinuity [12], asymptotic crack-tip functions for crack tip modeling [7], distance enrichment functions for weak discontinuities [10, 31] and hyperbolic tangent enrichment functions for discontinuities in derivatives [1]. Furthermore, The XFEM has successfully been applied to many other applications; cohesive crack models [24, 35], evolution of dislocations [16, 33] and modeling of grain boundaries [29]. In addition, XFEM and GFEM provided a crucial insight for meshless methods [27, 34] involving the dynamic fracture simulations. Although in these approaches, the extended approximation effectively captures the discontinuity, it may not be able to

reproduce the polynomial functions required for completeness.

One of the main difficulties that arises in using conventional XFEM is the choice of enrichment functions from which the discontinuities are captured [2]. Since based on the partition of unity (PU) property [12, 11], the extended interpolation can only reproduce the enrichment functions exactly, very accurate selection of these enrichment functions is crucial to maintain the accuracy of the results. Therefore, it is desirable to have an enrichment that can reproduce both the discontinuous function and the motions required for FE completeness.

Another challenge arisen in using XFEM is the implementation. In conventional XFEM, the enrichment part generally spreads over the elements contiguous to the enriched element. These elements are often called blending elements and should be treated appropriately [11]. For step enrichment functions, the blending regions can be avoided by shifting enrichment techniques as introduced by Zi and Belytschko [35]. Furthermore, in conventional XFEM, the enrichment parameters are assigned to element nodes which are often in common among several elements. However, this precludes the abstract description of enrichment part which can dramatically facilitates the XFEM implementation. Therefore, it is also desirable to have a technique that can define an enrichment displacement independent from element nodes.

The main objective of this work is to develop a highly efficient XFEM basis functions but nevertheless quite accurate formulation for dynamic fracture simulations. Such XFEM bases are defined to reproduce not only the discontinuity functions but the polynomials which are in turn required for completeness condition. In this method, the enrichment parameters are selected as *physically-based* quantities associated to the discontinuity of the problem whereby the Dirichlet boundary conditions can be simply imposed on both element edges and the surfaces of discontinuity. Moreover, the associated enrichment functions are constructed so that they vanish on element edges. This feature leads to an enrichment fully defined in a local domain,

which dramatically simplifies the XFEM implementation. Hence, it is conceivable to think that the proposed method can be an effective scheme for constructing enrichment functions in an XFEM framework.

The remaining chapters are organized as follows: Chapter 1 briefly reviews the conventional XFEM. Chapter 2 models a strong discontinuity, i.e. a crack, using a new methodology that exploits a set of non-nodal points for constructing the enrichment bases and then, Chapter 3 enhances such enrichment bases to capture the weak discontinuities, i.e. the discontinuities in the derivative of a function. Chapter 4 reviews the governing equations, weak formulation and discretization along with the cohesive models and a radial-return algorithm to compute the cohesive forces. Chapter 5 provides several numerical examples for crack propagation to demonstrate the efficacy and the robustness of the method. Finally, the last Chapter presents the conclusions and future works.

Chapter 1

Review of the Extended Finite Element Method

The finite element method (FEM) effectively approximates the solution of the partial differential equations (PDE) with piecewise differentiable polynomials. For this purpose, it first subdivides the body of the structure into segments that are called finite elements. Then, it approximates the solution within each element with polynomials. One advantage of the FEM is that it best approximates the solution within element whereby the solution converges to the exact solution with mesh refinement. However, the finite element approximations are not approximations well suited for problems with discontinuities. When the solution is discontinuous across an interface, the finite element mesh must also conform with the interface. This becomes computationally expensive for moving discontinuities, since the mesh must be updated whenever the discontinuity propagates.

The extended finite element method successfully models various discontinuities by extending the FE approximation such that it can best reflect the solution of the PDE. The enrichment part of the approximation consists of enrichment functions and enrichment parameters which are selected based on *a-priori* knowledge about the discontinuity. The main underlying key concepts in XFEM analysis are: partition of unity (PU) and level set functions which are described in more details in the following sections.

1.1 PARTITION OF UNITY

The partition of unity concept was first used in the enrichment definitions by Babuška et al. [3], which led to generalized finite element methods (GFEM). In this approach, a set of unity functions N_I is used to reproduce the discontinuous function Φ exactly by satisfying

$$\sum_{I=1}^{N} N_I(\mathbf{X})\Phi(\mathbf{X}) = \Phi(\mathbf{X}) \tag{1.1}$$

In GFEM, the partition of unity is applied to the entire domain [4, 22] and so would entail considerable computational cost. However, In XFEM, instead of a global partition of unity, a local discontinuous partition of unity that only spans throughout the enriched element is constructed [7, 25].

1.2 LEVEL SETS

We consider a two-dimensional domain $\Omega_0 \in R^2$ with its boundary Γ^0 in the reference configuration as shown in Figure 1.1. The material and spatial co-ordinates are denoted by $\mathbf{X}$ and $\mathbf{x}$, respectively and the motion is described by $\mathbf{x} = \mathbf{u}(\mathbf{X}, t)$. The current images of Ω_0 and Γ^0 are denoted by Ω and Γ, respectively. The entire boundary Γ^0 is partitioned into either the essential boundary Γ^0_{u} or the natural boundary Γ^0_{t} such that $\partial\Gamma^0_{\mathrm{u}} \cap \partial\Gamma^0_{\mathrm{t}} = \varnothing$ and $\partial\Gamma^0_{\mathrm{u}} \cup \partial\Gamma^0_{\mathrm{t}} = \Gamma^0$. In the XFEM framework, to construct

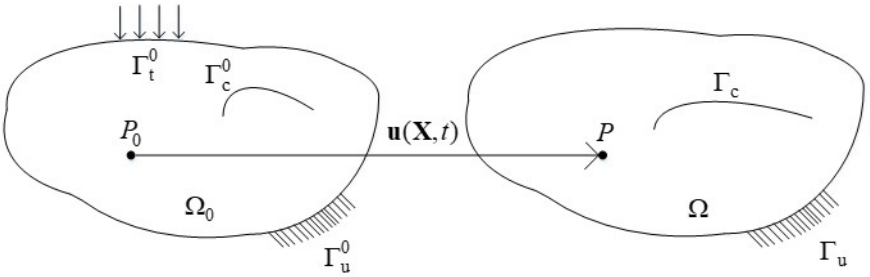

Figure 1.1 A two-dimensional domain and its current configuration with a crack.

enrichment functions, an accurate description of the interface is often useful. The interface, i.e. the crack surface in this study, can be implicitly defined by a set of level set functions as

$$\mathbf{X} \in \Gamma_c^0 \quad \text{if} \quad f(\mathbf{X}) = 0 \ \text{ and } \ g(\mathbf{X}, t) > 0 \tag{1.2}$$

As shown in Figure 1.2, the level set function f can be defined in terms of signed distance function given by

$$f(\mathbf{X}) = \min_{\bar{\mathbf{X}} \in \Gamma_c} \|\mathbf{X} - \bar{\mathbf{X}}\| \ \text{sign}(\mathbf{n}^+.(\bar{\mathbf{X}} - \mathbf{X})) \tag{1.3}$$

where $\bar{\mathbf{X}}$ is the closest point on the interface to $\mathbf{X}$ and $\|.\|$ denotes the Euclidean norm. The function $g(\mathbf{X}, t)$ is defined such that the crack is enclosed within the subdomain $g(\mathbf{X}, t) \geq 0$ whereby the crack tip is located by $g(\mathbf{X}, t) = 0$. For discretized domains, the evaluation of the implicit function $f(\mathbf{X})$ can be simplified by finite element discretization and is then defined by

$$f(\mathbf{X}) = \sum_I f_I N_I(\mathbf{X}) \tag{1.4}$$

Furthermore, the derivatives of the level set functions which are useful in the cohesive force computations can be simply computed by finite element approximations as

$$f_{,i}(\mathbf{X}) = \sum_I f_I N_{I,i}(\mathbf{X}) \tag{1.5}$$

The level set function defined in Equation (1.3) can be simply adopted to define various discontinuities. For example, a strong discontinuity in a function, i.e. a displacement jump in crack modeling, can be represented by either the sign distance function or the Heaviside step function. The sign distance function can be defined according to the level set function as

$$\text{sign}(f(\mathbf{X})) = \begin{cases} -1 & \text{if } f(\mathbf{X}) < 0 \\ +1 & \text{if } f(\mathbf{X}) > 0 \end{cases} \tag{1.6}$$

and the Heaviside step function can be written as

$$H(f(\mathbf{X})) = \begin{cases} 0 & \text{if } f(\mathbf{X}) < 0 \\ 1 & \text{if } f(\mathbf{X}) > 0 \end{cases} \tag{1.7}$$

In the next section, the extended interpolation used in conventional XFEM

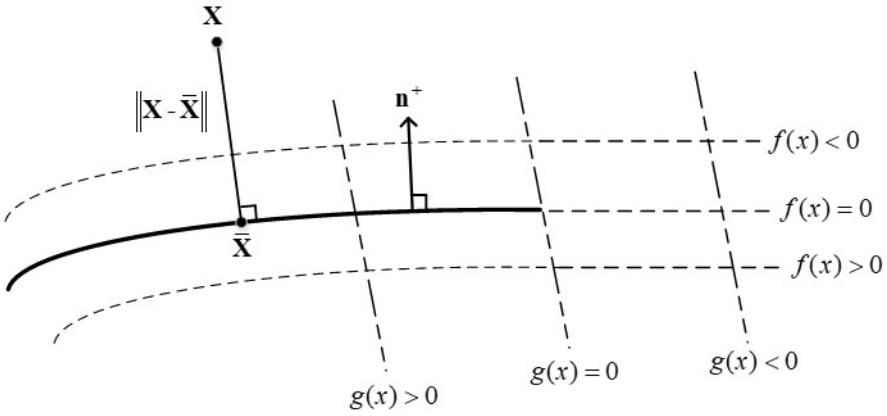

Figure 1.2 Crack representation by two level set functions f and g.

will be briefly introduced for crack modeling.

1.3 REPRESENTATION OF A DISCONTINUITY WITH STANDARD XFEM

In the following, we first describe the XFEM crack modeling in one dimension. Let us consider a bar with a crack as shown in Figure 1.3(a). The crack is located inside the middle element denoted by X_c and the nodes of element containing the crack are numbered 1 and 2. Considering the sign distance function as enrichment function, the standard XFEM description of the displacement field within an element is given by

$$\begin{aligned} \mathbf{u}(X,t) &= \mathbf{u}^{\text{cons}}(X,t) + \mathbf{u}^{\text{disc}}(X,t) \\ &= \sum_{I=1}^{2} N_I(X)\mathbf{u}_I(t) + \sum_{I=1}^{2} N_I(X)\text{sign}(X)\mathbf{q}_I(t) \end{aligned} \tag{1.8}$$

where $\mathbf{u}^{\text{cons}}$ and $\mathbf{u}^{\text{disc}}$ are continuous and discontinuous parts of the interpolation and $\mathbf{q}_I$ is the enrichment parameter associated to node I.

The continuous and discontinuous parts of the displacement are shown in Figure 1.3(a). As it can be seen, the enriched displacement field does not vanish at element nodes, i.e. the Kronekcer-δ property does not satisfy. As proposed in References [10, 35] the Kronecker-δ property can be achieved by shifting enrichment functions with respect to element nodes. The shifted enrichment functions are defined as

$$\Psi_I(X) = \text{sign}(X) - \text{sign}(X_{\text{I}}) \tag{1.9}$$

As it is shown in Figure 1.3(b), the shifted enrichment displacements vanish outside the element domain including the element nodes.

For a multi-dimensional problem, the XFEM approximation for an element

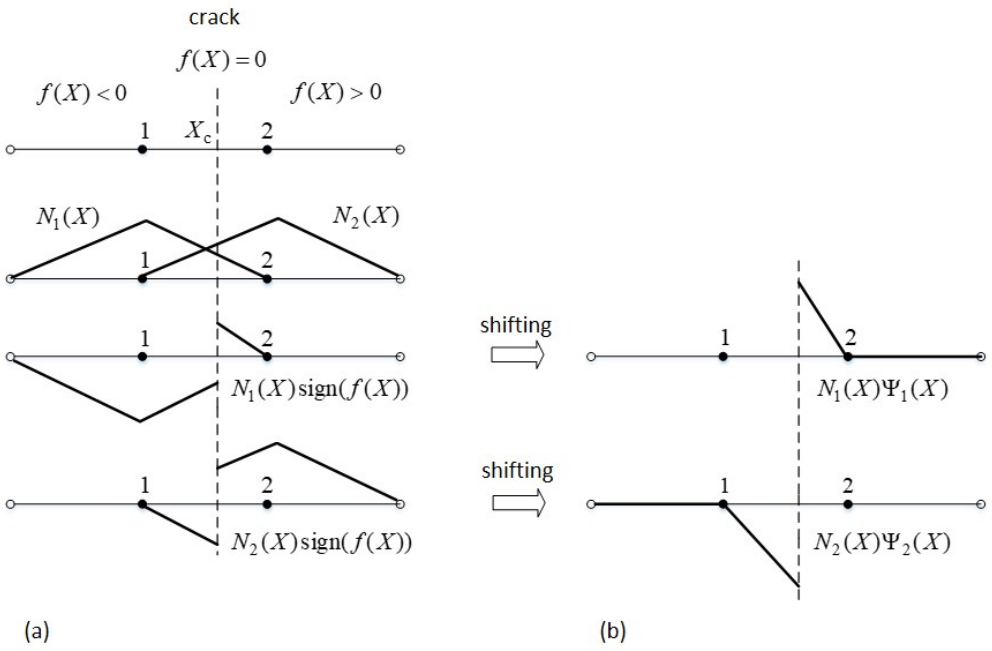

Figure 1.3 One-dimensional crack enrichment displacement: (a) enriched displacement without shifting enrichment functions; and (b) shifted enrichment displacement.

is expressed by

$$\mathbf{u}(\mathbf{X},t) = \sum_{J\in\delta} N_J(\mathbf{X})\mathbf{u}_J(t) + \sum_{K\in\varepsilon}\sum_{J\in\delta_c^K} N_J^K(\mathbf{X})\Psi_J^K(\mathbf{X})\mathbf{q}_J^K(t) \tag{1.10}$$

where δ is the set of all element nodes, ε the number of discontinuity surfaces, and δ_c^K the set of enrich nodes associated to the surface K. The enrichment function Ψ is obtained from the Equation (1.9).

Chapter 2

Enriched Displacement Fields for Discontinuity Using Non-Nodal Enrichment Parameters

In conventional XFEM, the discontinuous function itself is used as the enrichment function and the partition of unity enables the approximation to reproduce discontinuous functions exactly by satisfying the Equation (1.1). However, in the presented method, the enrichment functions are associated to the non-nodal points and are defined so that they can reproduce the discontinuity without local partition of unity, i.e. the enrichment functions are not multiplied by standard shape functions N_I, and consequently the element nodes are not enriched. In a vector form, the displacement field can then be defined as following:

$$\begin{aligned} \mathbf{u}(\mathbf{X},t) &= \mathbf{u}^{\text{cons}}(\mathbf{X},t) + \mathbf{u}^{\text{disc}}(\mathbf{X},t) \\ &= \sum_{I=1}^{N} N_I(\mathbf{X})\mathbf{u}_I(t) + \sum_{J\in\delta_{\text{en}}} \Psi_J(\mathbf{X})\mathbf{a}_J(t) \end{aligned} \tag{2.1}$$

where δ_{en} is the set of non-nodal enriched points (usually on crack path in two dimensions) and $\mathbf{a}_J$ are the additional degrees of freedom associated with their enrichment function Ψ_J.

In the following, first we will describe the crack modeling procedure in two dimensions for a constant strain triangular element, then introduce a general formulation independent from both the element type and the discontinuous function.

2.1 REPRESENTATION OF A CRACK WITH NON-NODAL ENRICHMENT PARAMETERS FOR THREE-NODE TRIANGULAR ELEMENTS

In this section, we will describe the crack modeling procedure in two dimensions for a constant strain triangular element. We only consider the elements that are completely cut by a crack, i.e., a crack propagates one complete element at a time so that the crack tip is always placed on element edges.

Let us consider a finite element with the local node numbers as shown in Figure 2.1(a). The crack is assumed to be straight within the element; it has advanced from the surface S_3 to the surface S_1 so that $\mathbf{X}_{c1}$ and $\mathbf{X}_{c2}$ are the first and second intersection points between the crack and element edges, respectively. The enrich-

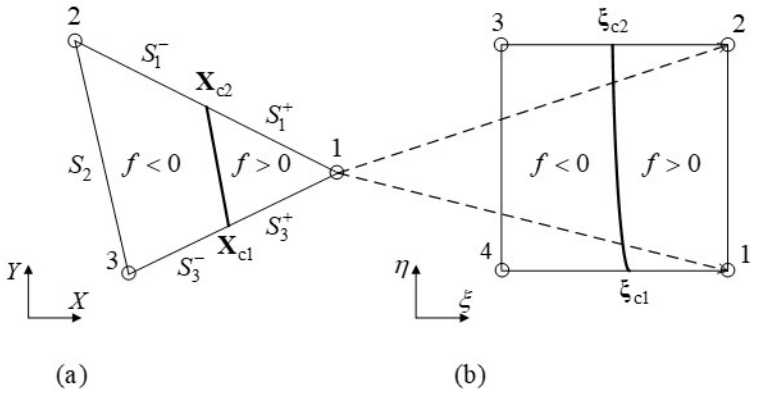

Figure 2.1 Duffy's mapping between (a) a triangular element in material coordinates and (b) a biunit square in parent coordinates $-1 \leq \xi \leq 1; -1 \leq \eta \leq 1$.

ment variables in crack modeling are considered the jump in the function, i.e. the displacement, at the non-nodal points; in Figure 2.1(a), the jump in displacement at $\mathbf{X}_{c1}$ and $\mathbf{X}_{c2}$ are denoted by $[\![\mathbf{u}]\!]_1$ and $[\![\mathbf{u}]\!]_2$, respectively. Thus, Equation (2.1) is

rewritten as:

$$\begin{aligned}\mathbf{u}(\mathbf{X},t) &= \sum_{I=1}^{3} N_I(\mathbf{X})\mathbf{u}_I(t) + \sum_{J\in\delta_{\text{en}}} \Psi_J(\mathbf{X})[\![\mathbf{u}(t)]\!]_J \\ &= \sum_{I=1}^{3} N_I(\mathbf{X})\mathbf{u}_I(t) + \Psi_1(\mathbf{X})[\![\mathbf{u}(t)]\!]_1 + \Psi_2(\mathbf{X})[\![\mathbf{u}(t)]\!]_2\end{aligned} \tag{2.2}$$

where the enrichment variables $[\![\mathbf{u}]\!]_1$ and $[\![\mathbf{u}]\!]_2$ are illustrated in Figure 2.2(a). We

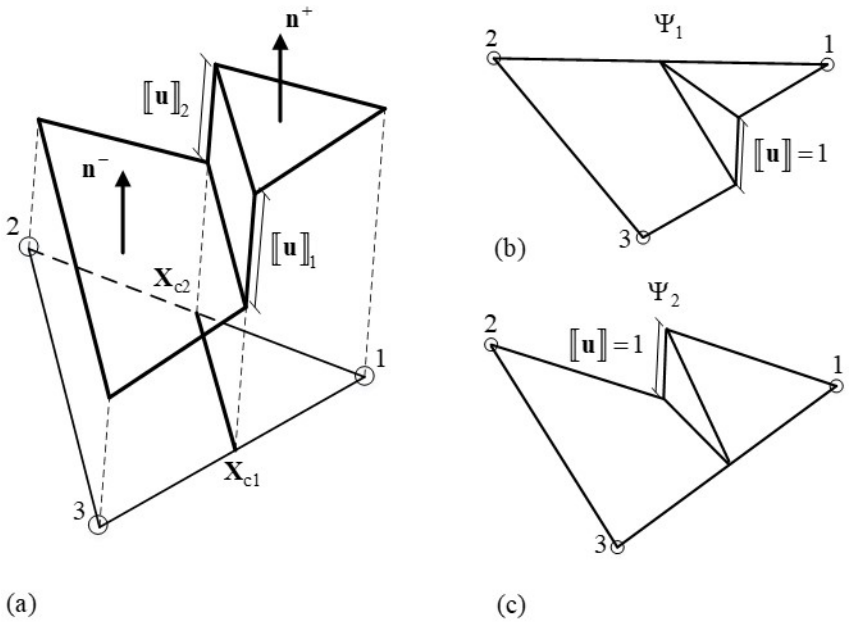

Figure 2.2 The enrichment parameters and their associated enrichment functions: (a) the representation of a discontinuity in a two-dimensional model; $\mathbf{n}^+$ and $\mathbf{n}^-$ are normal to the interpolation surfaces; (b) the first enrichment function associated to the non-nodal point $\mathbf{X}_{\text{c1}}$; and (c) the second enrichment function associated to the non-nodal point $\mathbf{X}_{\text{c2}}$.

construct the enrichment functions so that the extended interpolation in Equation (2.2) can reproduce the discontinuous function, i.e. the Heaviside step function in Equation (1.7). Thus, by substituting the displacement field $\mathbf{u}$ with the vectorized $\mathbf{H}$, the Equation (2.2) can be rewritten as

$$\mathbf{H}(\mathbf{X},t) = \sum_{I=1}^{3} N_I(\mathbf{X})\mathbf{H}_I + \Psi_1(\mathbf{X})[\![\mathbf{H}]\!]_1 + \Psi_2(\mathbf{X})[\![\mathbf{H}]\!]_2 \tag{2.3}$$

For the assumed direction of the crack illustrated in Figure 2.1(a), $\mathbf{H}_1 = 1$, $\mathbf{H}_2 = \mathbf{H}_3 = 0$ and $[\![\mathbf{H}]\!]_{\mathbf{X}\in\Gamma_c} = 1$. Considering $\sum_{I=1}^{3} N_I = 1$ and by partitioning Equation (2.3) for each side of the interface, we have

$$\begin{aligned} \Psi_1^+(\mathbf{X}) + \Psi_2^+(\mathbf{X}) &= N_2 + N_3 \\ \Psi_1^-(\mathbf{X}) + \Psi_2^-(\mathbf{X}) &= -N_1 \end{aligned} \tag{2.4}$$

It is important to note that finding a set of enrichment functions that satisfies Equation (2.4) enables the extended finite element interpolation to reproduce the discontinuous function. However, Equation (2.4) does not satisfy the C^0 continuity condition among enriched element and its contiguous elements. Therefore, to satisfy C^0 continuity conditions, the enrichment functions must vanish along specific element edges. For instance, in the first equation, Ψ_1^+ and Ψ_2^+ must vanish along surfaces S_1^+ and S_3^+ as shown in Figure 2.1, respectively. Thus, we simply assign $\Psi_1^+ = N_3$ and $\Psi_2^+ = N_2$. However in the second equation Ψ_1^- must vanish along both surfaces S_1^- and S_2, and also Ψ_2^- must vanish along surfaces S_3^- and S_2.

To facilitate the construction of such enrichment function, the Duffy's transformation which is a mapping between a triangle and a square can be used; the Duffy's transformation can be viewed as a mapping from a square in parent coordinates to a triangle in material coordinates as illustrated in Figure 2.1. A detailed description of the Duffy's transformation can be found in [13, 20, 26] .

In this transformation, one vertex in the triangle is mapped to an edge in the square; i.e. edge $\bar{12}$ in Figure 2.1(b). This vertex is chosen such that the crack passes through non-adjacent edges in parent domain. Therefore, this node should be the node opposite to the edge that is not intersected by the crack, which is node 1 here (See Figure 2.1). Then, the FE approximation is given by

$$\mathbf{u}(\mathbf{X}, t) = \sum_{I=1}^{3} N_I^{'}(\mathbf{X})\mathbf{u}_I(t) \tag{2.5}$$

where the Duffy's isoparametric shape functions can be expressed in terms of standard bilinear shape functions

$$\begin{aligned} N_1' &= N_1^{4Q} + N_2^{4Q} \\ N_2' &= N_3^{4Q} \\ N_3' &= N_4^{4Q} \end{aligned} \tag{2.6}$$

where

$$N_I^{4Q}(\xi, \eta) = \frac{1}{4}(1 + \xi_I \xi)(1 + \eta_I \eta) \tag{2.7}$$

Here, (ξ_I, η_I) are nodal coordinates of bi-unit square in parent coordinates shown in Figure 2.1(b). By substituting the shape functions in Equation (2.6) into Equation (2.4), we can obtain

$$\begin{aligned} \Psi_1^+(\mathbf{X}) + \Psi_2^+(\mathbf{X}) &= N_3^{4Q} + N_4^{4Q} \\ \Psi_1^-(\mathbf{X}) + \Psi_2^-(\mathbf{X}) &= -N_1^{4Q} - N_2^{4Q} \end{aligned} \tag{2.8}$$

Thus, the C^0 continuity is simply satisfied by assigning the enrichment functions as follows

$$\begin{aligned} \Psi_1^+ &= N_4^{4Q} \\ \Psi_1^- &= -N_1^{4Q} \\ \Psi_2^+ &= N_3^{4Q} \\ \Psi_2^- &= -N_2^{4Q} \end{aligned} \tag{2.9}$$

It is important to note that the enrichment functions obtained by the Duffy's transformation are in terms of well-known bilinear shape functions. So, one can extensively make use of existing codes for the computation of the enrichment functions and their derivatives. However, some more code implementation is required to implement the Duffy's interpolation.

The enrichment functions in Equation (2.9) are shown in Figure 2.2(b)-(c). As it can be seen, the enrichment functions have a jump equal to the unity at their associated non-nodal enrichment point. Since the linear shape functions of three-node triangular elements are higher order than the constant discontinuous function, the

interpolation in Equation (2.2), in addition to the Heaviside step function, can reproduce two parallel planes at both sides of the interface; two planes shown in Figure 2.2(a) that their unit normal to the surface of the interpolation are parallel to each other, i.e.

$$\mathbf{n}^+ \times \mathbf{n}^- = \mathbf{0} \tag{2.10}$$

The detailed proof has been provided in Appendix A, and the relation between bilinear Duffy shape functions and the standard triangle shape functions is described in Appendix B. Thus, the enrichment functions in Equation 2.9 can be described by standard shape functions as

$$\begin{aligned} \Psi_1^+ &= N_3 \\ \Psi_1^- &= -\frac{N_1 \times N_3}{N_2 + N_3} \\ \Psi_2^+ &= N_2 \\ \Psi_2^- &= -\frac{N_1 \times N_2}{N_2 + N_3} \end{aligned} \tag{2.11}$$

2.2 GENERAL FORMULATION OF THE NON-NODAL ENRICHMENT XFEM

In this section, we describe the method for a multi-node element with a general discontinuous function $\Phi(\mathbf{X})$. The discontinuous function can be defined as a function of level set function as

$$\Phi(\mathbf{X}) = F(f(\mathbf{X})) \tag{2.12}$$

As discussed in previous section, Equation (2.1) can reproduce the discontinuous function Φ, if it holds for $\mathbf{u} = \Phi$. Thus, Equation (2.1) gives

$$\Phi(\mathbf{X}) = \sum_{I=1}^{n_e} N_I(\mathbf{X})\Phi(\mathbf{X}_I) + \sum_{J \in \delta_{en}} \Psi_J(\mathbf{X})\mathbf{a}_J \tag{2.13}$$

By rewriting Equation (2.13) for either side of the interface separately we have

$$\begin{aligned} \Phi^+(\mathbf{X}) &= \sum_{I=1}^{n_e} N_I(\mathbf{X})\Phi(\mathbf{X}_I) + \sum_{J \in \delta_{en}} \Psi_J^+(\mathbf{X})\mathbf{a}_J \\ \Phi^-(\mathbf{X}) &= \sum_{I=1}^{n_e} N_I(\mathbf{X})\Phi(\mathbf{X}_I) + \sum_{J \in \delta_{en}} \Psi_J^-(\mathbf{X})\mathbf{a}_J \end{aligned} \tag{2.14}$$

The first terms on the right-hand side of Equation (2.14) can also be partitioned for nodes at either side of the interface as

$$\sum_{I=1}^{n_e} N_I(\mathbf{X})\Phi(\mathbf{X}_I) = \sum_{I\in\delta_n^-} N_I(\mathbf{X})\Phi^-(\mathbf{X}_I) + \sum_{I\in\delta_n^+} N_I(\mathbf{X})\Phi^+(\mathbf{X}_I) \tag{2.15}$$

where δ_n^+ and δ_n^- are the sets of element nodes that are on the subdomains where $f > 0$ and $f < 0$, respectively.

In this study, we assume that the discontinuous functions at either side of the interface, i.e. Φ^+ and Φ^- are as sufficiently smooth as to be interpolated by standard shape functions. For example, the strong and weak discontinuities are often approximated with the Heaviside and distance functions, respectively. This indicates that the enrichment functions are constant or linear on both sides of the interface and therefore, can be exactly interpolated by linear shape functions. Thus, Φ^+ and Φ^- can be described in terms of standard shape functions by

$$\begin{aligned} \Phi^+(\mathbf{X}) &= \sum_{I=1}^{n_e} N_I(\mathbf{X})\Phi^+(\mathbf{X}_I) \\ \Phi^-(\mathbf{X}) &= \sum_{I=1}^{n_e} N_I(\mathbf{X})\ \Phi^-(\mathbf{X}_I) \end{aligned} \tag{2.16}$$

Substituting Equations (2.15) and (2.16) into (2.14), we will have

$$\begin{aligned} \sum_{I\in\delta_n^-} N_I(\mathbf{X})[\![\Phi]\!]_{\mathbf{X}=\mathbf{X}_I} &= \sum_{J\in\delta_{\text{en}}} \Psi_J^+(\mathbf{X})\mathbf{a}_J \\ \sum_{I\in\delta_n^+} -N_I(\mathbf{X})[\![\Phi]\!]_{\mathbf{X}=\mathbf{X}_I} &= \sum_{J\in\delta_{\text{en}}} \Psi_J^-(\mathbf{X})\mathbf{a}_J \end{aligned} \tag{2.17}$$

where $[\![\Phi]\!]_{\mathbf{X}} = \Phi^+(\mathbf{X}) - \Phi^-(\mathbf{X})$ is the jump in function at $\mathbf{X}$. Note that Equations (2.17) are the key equations used to construct the enrichment functions. It must be stressed that these equations do not suffice to provide closure to the definition of the enrichment functions. In other words, there are no unique enrichment functions and enrichment parameters that satisfy Equations (2.17). The overall procedure to define the enrichments can be organized using the following main steps:

1. Identifying the discontinuity in the problem (denoted by Φ here) using a-priori knowledge about the discontinuity in the problem.

2. Introducing the enrichment parameters which are best able to represent the identified discontinuity.

3. Defining the minimum number of enrichment parameters and their associated enrichment functions to satisfy the following conditions:

   a) Equation(2.17)

   b) The C^0 continuity condition between the enriched element and contiguous elements.

Note that the enrichment functions for triangular elements obtained in previous section can be simply attained using the aforementioned procedure. As an example, the crack modeling in one dimension has been demonstrated, in general, using Equation (2.17) in Appendix C.

2.3 COMPARISON TO CONVENTIONAL XFEM

Some methodological issues of the conventional XFEM addressed by the non-nodal enrichment method are briefly described here:

- The local partition of unity given in Equation (1.1) only builds a partition of unity over reproducing elements for which all element nodes are enriched; see References [11, 14, 15, 32] for more details. Due to mesh constrains, some of the element nodes may not be enriched for an element completely cut by a crack; these elements are often called blending elements. An example has been depicted in Figure 2.3, where a crack has advanced through several elements and the crack tip is on the intersection of elements e_4 and e_5. To satisfy C^0 continuity condition, the nodes placed on the crack tip edge are selected not to be enriched as follows in Figure 2.3, which leads to an unenriched node I. Thus, although the crack has crossed over the elements e_1 through e_4, these elements

are not still reproducing elements. In contrast to conventional XFEM, in non-nodal enrichment method, as soon as the crack passes through the element, it becomes a reproducing element.

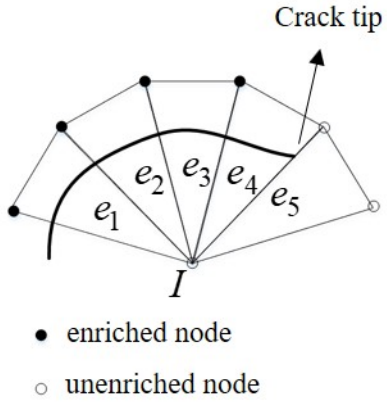

Figure 2.3 A crack path on several elements which are not still reproducing elements because the enrichment is not added to node I.

- The conventional XFEM approximations do not, in general, satisfy the Kronecker-δ property that leads to difficulties in imposition of Dirichlet boundary conditions on enriched nodes. As proposed in References [35, 10], the Kronecker-δ property can be achieved by shifting enrichment functions with respect to element nodes. However, shifting enrichment functions renders the construction of lumped mass matrix difficult which is crucial for efficient dynamic analysis. In the proposed method, the enrichment functions are vanished on element edges and consequently the Kronecker-δ property is essentially satisfied.

- Although the shifted enrichment functions hold the Kronecker-δ property, they may not vanish on contiguous elements. This may influence the imposition of Dirichlet boundary conditions on element edges. Moreover, to preclude the

parasitic terms added to the approximation, the contiguous elements which are blending elements are required to be treated appropriately. However, in the proposed method, the enrichment functions are vanished outside the element domains and consequently no blending elements appear.

- In conventional XFEM, the interpretation of the enrichment parameters is difficult so that the non-smooth Dirichlet boundary conditions and interface conditions may not be easily imposed on enrichment parameters. One of the main Dirichlet boundary conditions imposed on contact interface is impenetrability condition. In non-nodal enrichment method, the impenetrability condition can be easily applied as a Dirichlet boundary conditions in strong form as

$$\text{if} \quad [\![\mathbf{u}]\!] = 0, \quad [\![\dot{\mathbf{u}}]\!].\mathbf{n} \geq 0 \tag{2.18}$$

- In the conventional XFEM, the enriched nodes are chosen based on both the direction of the crack growth and whether it is contiguous to an existing crack or not. As shown in Figure 2.4(a)-(b), the set of enriched nodes is dependent on the crack directions. However, in the presented method, enriching procedure depends on neither the crack direction nor the elements contiguous to the enriched element which indeed facilitates the crack modeling in an object-oriented program. As shown in Figure 2.4(c)-(d), wherever a crack passes over an edge, one enrichment variables assigned to the intersection point is added to the enrichment variable set.

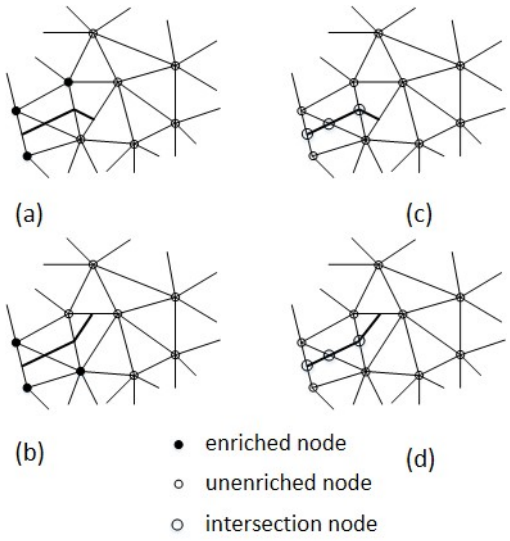

Figure 2.4 Selection of enriched nodes: (a)-(b) in the conventional XFEM where enriched nodes are dependent on the direction of crack; and (c)-(d) in the proposed method where the FE nodes are not enriched but for each intersection point two enrichment variables are additionally defined.

Chapter 3

Linear Complete Enriched Displacement Fields for Discontinuity

In this section, we extend the interpolation so that it can capture two discontinuities: a strong discontinuity across the crack surface which can be represented with a jump in the displacement and a weak discontinuity which can be considered a jump in the strains. It can be shown that when the interpolation reproduces independent linear functions on sides of the interface, then such discontinuities can be captured. Therefore, the interpolation is enriched to reproduce two discontinuities across the interface; a strong discontinuity at a function denoted by Φ^{u} and a weak discontinuity at its first derivative denoted by $\Phi^{\nabla \mathrm{u}}$. The strong discontinuity is given in Equation (1.7) and the weak discontinuity can also be defined by adopting the Heaviside step function as

$$\Phi^{\nabla \mathrm{u}} = H(f(\mathbf{X})) \times f(\mathbf{X}) = \begin{cases} 0 & \text{if } f(\mathbf{X}) < 0 \\ f(\mathbf{X}) & \text{if } f(\mathbf{X}) > 0 \end{cases} \tag{3.1}$$

The discontinuous functions Φ^{u} and $\Phi^{\nabla \mathrm{u}}$ are plotted in one dimension in Figure 3.1.

To capture such discontinuities, two enrichment functions Ψ^{u} and $\Psi^{\nabla \mathrm{u}}$ are associated to the *physically-based* enrichment variables: jump in the displacement $[\![u]\!]$ and jump in the gradient of the displacement $[\![L^e \nabla u]\!]$, respectively. The latter is consciously multiplied by L^e to make the units of nodal values consistent which significantly reduces the condition numbers of stiffness matrix.

In the following, we first construct the non-nodal enrichment parts in one dimension, then for a linear triangular element in two dimensions.

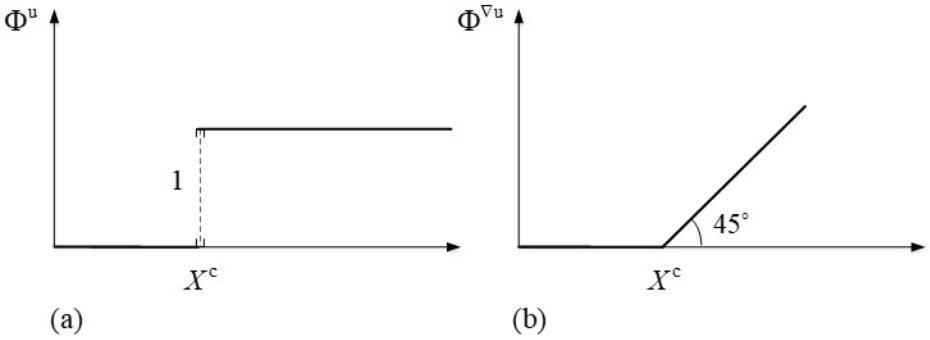

Figure 3.1 Representation of the discontinuity in: (a) a function; and (b) a derivative of a function.

3.1 REPRESENTATION OF A CRACK WITH NON-NODAL ENRICHMENT PARAMETERS FOR 2-NODE LINEAR ELEMENTS

Let us consider a one-dimensional bar with a strong discontinuity, i.e. a crack, at $X = X^{c}$ as shown in Figure 3.2. The level set function f is considered negative and positive on the left side and right side of the crack, respectively. Figure 3.2(a) illustrates an arbitrary displacement field consisting two independent linear fields on sides of the interface. Such displacement fields can be reproduced by adding three independent parts: (i) a continuous displacement represented by finite element interpolation shown in Figure 3.2(b); (ii) a jump in the displacement captured by the enrichment function Ψ^{u} illustrated in Figure 3.2(c); and (iii) a jump in strain captured by the enrichment function $\Psi^{\nabla u}$ illustrated in Figure 3.2(d). It is important to note that the number of unknown variables to define two independent lines is $2 \times 2 = 4$, which is equal to the variables used here $\{u_1, u_2, [\![u]\!], [\![L^e \nabla u]\!]\}$.

Thus, the displacement field is then given by

$$\begin{aligned} \mathbf{u}(\mathbf{X}, t) &= \mathbf{u}^{\text{cons}}(\mathbf{X}, t) + \mathbf{u}^{\text{disc}}(\mathbf{X}, t) \\ &= \sum_{I=1}^{2} N_I(\mathbf{X}) \mathbf{u}_I(t) + \Psi^{u}(X) [\![u(t)]\!]_{X=X^{c}} + \Psi^{\nabla u}(X) [\![L^e \nabla u(t)]\!]_{X=X^{c}} \end{aligned} \tag{3.2}$$

The enrichment functions are constructed so that the Equation (3.2) can reproduce

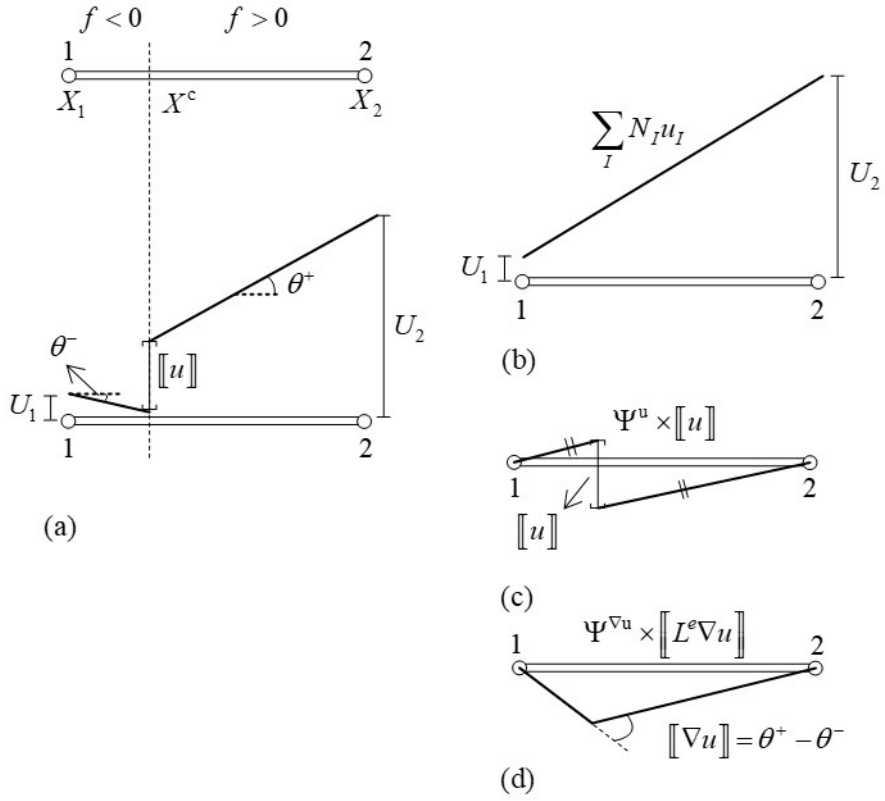

Figure 3.2 One-dimensional enrichment displacement fields: (a) an arbitrary linear displacement field on both sides of the crack; (b) the finite-element displacement field u^{FEM}; (c) the enrichment displacement field produced by displacement jump enrichment $\Psi^{\mathrm{u}} \times [\![u]\!]$; and (d) enrichment displacement field for gradient jump enrichment $\Psi^{\nabla \mathrm{u}} \times [\![L^e \nabla u]\!]$. Note that in one dimension for small derivatives $[\![\nabla u]\!] = [\![\epsilon]\!] = [\![\theta]\!] = \theta^+ - \theta^-$

the discontinuous functions in Equations (1.7) and (3.1).

Let us first consider the displacement field $u = \Phi^{\mathrm{u}}$, for which the Equation (3.2) for each side of the crack is simplified as

$$\begin{aligned} \Psi^{\mathrm{u}+} &= N_1 \\ \Psi^{\mathrm{u}-} &= -N_2 \end{aligned} \tag{3.3}$$

where for such a displacement, $[\![\Phi^{\mathrm{u}}]\!]_{X=X^{\mathrm{c}}} = 1$ and $[\![\nabla \Phi^{\mathrm{u}}]\!]_{X=X^{\mathrm{c}}} = 0$ (see Figure 3.1(a)). Note that the enrichment function Ψ^{u} is identical to the enrichment function obtained

in Equation (C.2), as expected. Next, considering the displacement $u = \Phi^{\nabla u}$, the Equation (3.2) is then simplified as

$$\begin{aligned} X - X^{c} &= N_2(X_2 - X^{c}) + L^{e}\Psi^{\nabla u+}(X) \\ 0 &= N_2(X_2 - X^{c}) + L^{e}\Psi^{\nabla u-}(X) \end{aligned} \tag{3.4}$$

For such a displacement, $[\![\Phi^{u}]\!]_{X=X^{c}} = 0$ and $[\![\Phi^{\nabla u}]\!]_{X=X^{c}} = 1$ (see Figure 3.1(b)). The term $X - X^{c}$ can be interpolated exactly by finite element interpolation as $X - X^{c} = \sum_{I=1}^{2} N_I(X_I - X^{c})$, so the Equation (3.4) gives the second enrichment function as follows

$$\begin{aligned} \Psi^{\nabla u+} &= -sN_1 \\ \Psi^{\nabla u-} &= -(1-s)N_2 \end{aligned} \tag{3.5}$$

where we have used a normalized parameter for the crack position defined as $s = (X^{c} - X_1)/L^{e}$. The enrichment functions have been plotted in Figure 3.3. Using these enrichment functions, the extended interpolation can reproduce two independent linear functions at sides of the crack. The classical proof has been provided in Appendix D.

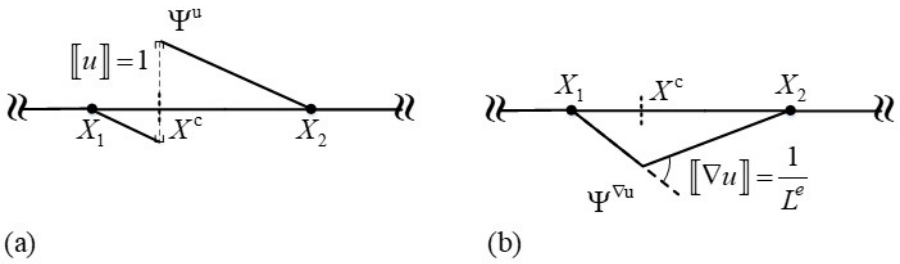

Figure 3.3 One-dimensional crack enrichment functions: (a) Ψ^{u}; and (b) $\Psi^{\nabla u}$.

3.2 REPRESENTATION OF A CRACK WITH NON-NODAL ENRICHMENT PARAMETERS FOR THREE-NODE TRIANGULAR ELEMENTS

Let us consider a triangular element that is completely cut by a crack as shown in Figure 3.4(a). For such a crack position, the strong and weak discontinuous functions given in Equations (1.7) and (3.1) are shown in Figures 3.4(b)-(c). The enrichment variables for capturing the strong discontinuity are chosen to be the displacement jump at the intersection points of the crack and element edges, which are the displacement jumps at $\mathbf{X}_1^{\mathrm{c}}$ and $\mathbf{X}_2^{\mathrm{c}}$ denoted by $[\![u]\!]_1$ and $[\![u]\!]_2$, respectively. Furthermore, the enrichment variables for capturing the weak discontinuity are selected to be the jump in directional derivative of the displacement at the intersection points.

To meet the C^0 continuity condition between the enriched element and its contiguous elements, the element edges at the intersection points are selected as the direction of derivatives. These directions are denoted by $\mathbf{e}_1^{\mathrm{c}}$ and $\mathbf{e}_2^{\mathrm{c}}$ as shown in Figure 3.5. So, the approximation of a scalar variable $u(\mathbf{X})$ is given by

$$\begin{aligned}\mathbf{u}(\mathbf{X}) &= \mathbf{u}^{\mathrm{cons}}(\mathbf{X}) + \mathbf{u}^{\mathrm{disc}}(\mathbf{X}) \\ &= \sum_{I=1}^{3} N_I(\mathbf{X})\mathbf{u}_I + \sum_{J\in\delta^{\mathrm{u}}} \Psi_J^{\mathrm{u}}(\mathbf{X})[\![u]\!]_J + \sum_{K\in\delta^{\nabla\mathrm{u}}} \Psi_K^{\nabla\mathrm{u}}(\mathbf{X})[\![L_K^{\mathrm{c}}\nabla u.\mathbf{e}_K^{\mathrm{c}}]\!]_K\end{aligned} \tag{3.6}$$

where δ^{u} and $\delta^{\nabla\mathrm{u}}$ are two sets including enriched discontinuous points on the interface, L_K^{c} is the length of an element edge that contains the point X_K^{c} and $[\![\nabla u.\mathbf{e}_K^{\mathrm{c}}]\!]_K$ is the jump in directional derivative along $\mathbf{e}_K^{\mathrm{c}}$ at X_K^{c}. In the following, we only consider the case that the element is completely cut by a crack, i.e. $\delta^{\mathrm{u}} = \delta^{\nabla\mathrm{u}} = \{1, 2\}$.

As discussed for one dimensional case, we wish to construct the enrichment functions so that the extended interpolation given by Equation (3.6) reproduces the discontinuous functions Φ^{u} and $\Phi^{\nabla\mathrm{u}}$. Let us first consider a displacement field equal to the Heaviside step function, i.e. $u = \Phi^{\mathrm{u}}$. For such a displacement field, the regular and enriched degrees of freedom (DOF) for the crack position shown in Figure 3.4(a) are obtained as

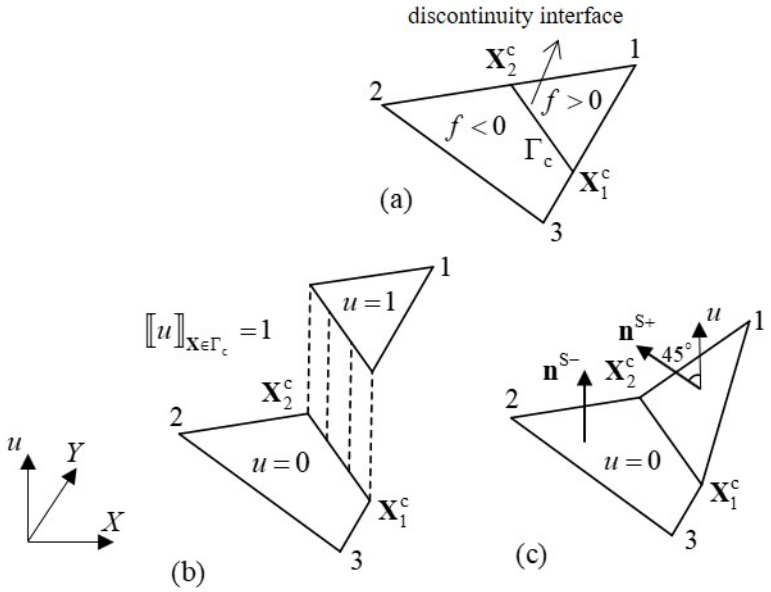

Figure 3.4 A strong discontinuity in two dimensions: (a) a triangular element with a crack; (b) Φ^{u}; and (c) $\Phi^{\nabla \mathrm{u}}$.

$$\text{Regular DOFs:} \begin{cases} \Phi_1^{\mathrm{u}} = 1 \\ \Phi_2^{\mathrm{u}} = 0 \\ \Phi_3^{\mathrm{u}} = 0 \end{cases} \qquad \text{Enriched DOFs:} \begin{cases} [\![\Phi^{\mathrm{u}}]\!]_1 = 1 \\ [\![L_1^{\mathrm{c}} \nabla \Phi^{\mathrm{u}}.\mathbf{e}_1^{\mathrm{c}}]\!]_1 = 0 \\ [\![\Phi^{\mathrm{u}}]\!]_2 = 1 \\ [\![L_2^{\mathrm{c}} \nabla \Phi^{\mathrm{u}}.\mathbf{e}_2^{\mathrm{c}}]\!]_2 = 0 \end{cases} \tag{3.7}$$

As it can be noted, for the Heaviside step function, the jumps in derivatives are vanished. Thus, the interpolation in Equation (3.6) reduces to the interpolation describe in Equation (2.2), and consequently the same enrichment functions are obtained de-

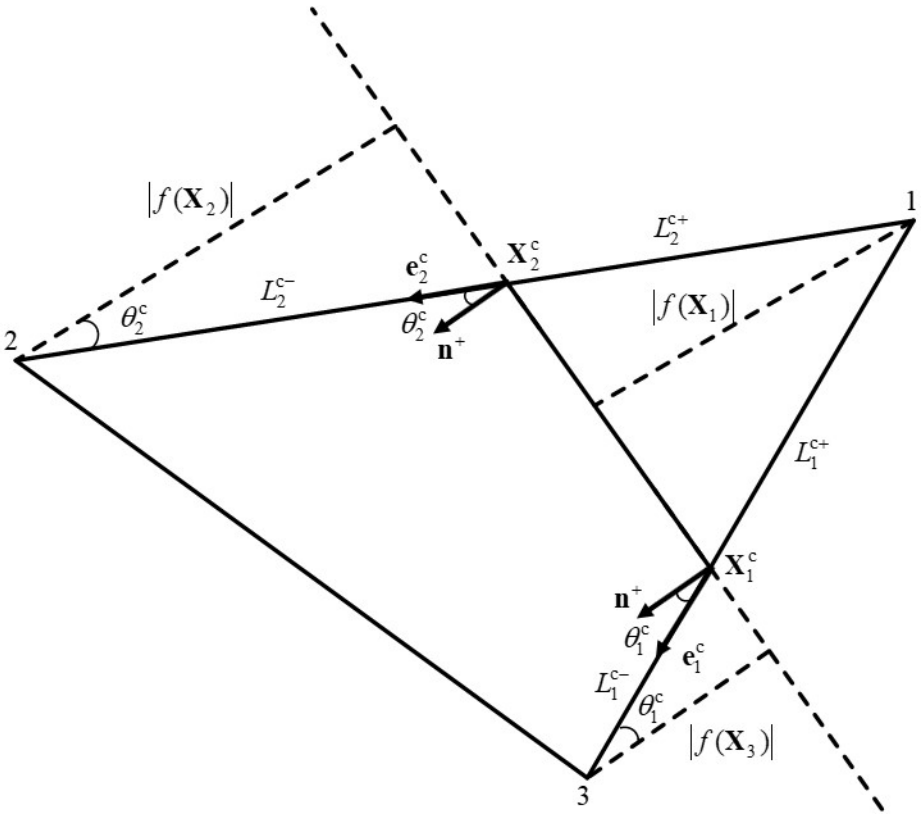

Figure 3.5 Illustration of nomenclature for a linear complete non-nodal enrichment in two dimension.

scribed here as

$$\Psi_1^{\mathrm{u}} = \begin{cases} -N_1^{4\mathrm{Q}} & f < 0 \\ N_4^{4\mathrm{Q}} & f > 0 \end{cases}$$
$$\Psi_2^{\mathrm{u}} = \begin{cases} -N_2^{4\mathrm{Q}} & f < 0 \\ N_3^{4\mathrm{Q}} & f > 0 \end{cases} \tag{3.8}$$

where the bilinear shape functions were resulted from the Duffy's transformation (see the Section 2.1 for more details). Next, considering the displacement field $u = \Phi^{\nabla \mathrm{u}}$,

the nodal values are determined as

$$\text{Regular DOFs:} \begin{cases} \Phi_1^{\nabla \mathrm{u}} & = f(\mathbf{X}_1) \\ \Phi_2^{\nabla \mathrm{u}} & = 0 \\ \Phi_3^{\nabla \mathrm{u}} & = 0 \end{cases} \qquad \text{Enriched DOFs:} \begin{cases} [\![\Phi^{\nabla \mathrm{u}}]\!]_1 & = 0 \\ [\![L_1^{\mathrm{c}} \nabla \Phi^{\nabla \mathrm{u}}.\mathbf{e}_1^{\mathrm{c}}]\!]_1 & = L_1^{\mathrm{c}} \dfrac{|f(\mathbf{X}_3)|}{L_1^{\mathrm{c}-}} \\ [\![\Phi^{\nabla \mathrm{u}}]\!]_2 & = 0 \\ [\![L_2^{\mathrm{c}} \nabla \Phi^{\nabla \mathrm{u}}.\mathbf{e}_2^{\mathrm{c}}]\!]_2 & = L_2^{\mathrm{c}} \dfrac{|f(\mathbf{X}_2)|}{L_2^{\mathrm{c}-}} \end{cases} \tag{3.9}$$

where for such a displacement $\nabla \Phi^{\nabla \mathrm{u}} = \mathbf{n}^+$ as depicted in Figure 3.5. By substituting the nodal values in Equation (3.7) in approximation given in Equation (3.6) and rewriting for each side of the interface, we have

$$\begin{aligned} f(\mathbf{X}) &= N_1 f(\mathbf{X}_1) + \Psi_1^{\nabla \mathrm{u}+} L_1^{\mathrm{c}} \frac{|f(\mathbf{X}_3)|}{L_1^{\mathrm{c}-}} + \Psi_2^{\nabla \mathrm{u}+} L_2^{\mathrm{c}} \frac{|f(\mathbf{X}_2)|}{L_2^{\mathrm{c}-}} \\ 0 &= N_1 f(\mathbf{X}_1) + \Psi_1^{\nabla \mathrm{u}-} L_1^{\mathrm{c}} \frac{|f(\mathbf{X}_3)|}{L_1^{\mathrm{c}-}} + \Psi_2^{\nabla \mathrm{u}-} L_2^{\mathrm{c}} \frac{|f(\mathbf{X}_2)|}{L_2^{\mathrm{c}-}} \end{aligned} \tag{3.10}$$

Since the function f is a linear function, it can be exactly interpolated by standard shape functions as $f = \sum_{I=1}^{3} N_I f_I$. For simplicity, we will define two normalized parameters for the first and second intersection points of the crack and element edges as $s_1 = L_1^{\mathrm{c}-}/L_1^{\mathrm{c}}$ and $s_2 = L_2^{\mathrm{c}-}/L_2^{\mathrm{c}}$, respectively. Exploiting the Duffy's transformation, the enrichment functions $\Psi_1^{\nabla u}$ and $\Psi_2^{\nabla u}$ are obtained as

$$\begin{aligned} \Psi_1^{\nabla \mathrm{u}} &= \begin{cases} -(1-s_1) N_1^{4\mathrm{Q}} & f < 0 \\ -s_1 N_4^{4\mathrm{Q}} & f > 0 \end{cases} \\ \Psi_2^{\nabla \mathrm{u}} &= \begin{cases} -(1-s_2) N_2^{4\mathrm{Q}} & f < 0 \\ -s_2 N_3^{4\mathrm{Q}} & f > 0 \end{cases} \end{aligned} \tag{3.11}$$

where we have used the side-splitter theorem.

It is important to note that the enrichment functions are defined so that the C^0 continuity condition is satisfied. Using the enrichment functions Ψ_J^{u} and $\Psi_J^{\nabla \mathrm{u}}$, the approximation in Equation (3.2) can reproduce two independent planes at either side of the crack. The detailed proof has been provided in Appendix E.

In this section, we will derive the enrichment function for a multi-node element with a discontinuity in the rth derivative of a function denoted by $\Phi^{(r)}(\mathbf{X})$, which occurs across the interface defined by $f(\mathbf{X}) = 0$. Thus, it can be described in terms of level set function as follows

$$\Phi_r(\mathbf{X}) = H(f(\mathbf{X})) \times f^r(\mathbf{X}) \tag{3.12}$$

The non-nodal approximation for capturing the discontinuous function $\Phi^{(r)}(\mathbf{X})$ is expressed by

$$u(\mathbf{X}) = \sum_{I=1}^{n_e} N_I(\mathbf{X}) u_I + \sum_{J \in \delta^r} \Psi^r_J(\mathbf{X}) a^r_J \tag{3.13}$$

where δ^r is a set of non-nodal points on the interface and Ψ^r_J and a^r_J are the enrichment function and enrichment parameter associated to point J. The enrichment parameter a^r_J can be defined as

$$a^r_J = \text{mes}(\Omega^e) \overline{n_{\text{SD}}}^{r} [\![\nabla u_{,r} . \mathbf{e}^{\text{c}}_J]\!]_J \tag{3.14}$$

where $\text{mes}(\Omega^e)$ is the measure of the domain (length in 1D, area in 2D or volume in 3D), n_{SD} is the number of spatial dimensions and $\nabla u_{,r}$ is defined as

$$\nabla u_{,r} = \begin{bmatrix} \dfrac{\partial^r u}{\partial X^r} \\ \\ \dfrac{\partial^r u}{\partial Y^r} \end{bmatrix} \tag{3.15}$$

The approximation described in Equation (3.13) must hold for the discontinuity given in Equation (3.12), i.e. $u = \Phi^{(r)}$. So

$$\Phi^{(r)}(\mathbf{X}) = \sum_{I=1}^{n_e} N_I(\mathbf{X}) \Phi^{(r)}_I + \sum_{J \in \delta^r} \Psi^r_J(\mathbf{X}) \times \text{mes}(\Omega^e) \overline{n_{\text{SD}}}^{r} [\![\nabla \Phi^{(r)}_{,r} . \mathbf{e}^{\text{c}}_J]\!]_J \tag{3.16}$$

By rewriting Equation (3.16) for either side of the interface separately we have

$$\begin{aligned} \Phi^{(r)+}(\mathbf{X}) &= \sum_{I=1}^{n_e} N_I(\mathbf{X}) \Phi^{(r)}_I + \sum_{J \in \delta^r} \Psi^{r+}_J(\mathbf{X}) \times \text{mes}(\Omega^e) \overline{n_{\text{SD}}}^{r} [\![\nabla \Phi^{(r)}_{,r} . \mathbf{e}^{\text{c}}_J]\!]_J \\ \Phi^{(r)-}(\mathbf{X}) &= \sum_{I=1}^{n_e} N_I(\mathbf{X}) \Phi^{(r)}_I + \sum_{J \in \delta^r} \Psi^{r-}_J(\mathbf{X}) \times \text{mes}(\Omega^e) \overline{n_{\text{SD}}}^{r} [\![\nabla \Phi^{(r)}_{,r} . \mathbf{e}^{\text{c}}_J]\!]_J \end{aligned} \tag{3.17}$$

The first terms on the right-hand side of Equation (3.17) can also be partitioned for nodes at either side of the interface as

$$\sum_{I=1}^{n_e} N_I(\mathbf{X})\Phi^{(r)}(\mathbf{X}_I) = \sum_{I\in\delta_n^-} N_I(\mathbf{X})\Phi^{(r)-}(\mathbf{X}_I) + \sum_{I\in\delta_n^+} N_I(\mathbf{X})\Phi^{(r)+}(\mathbf{X}_I) \tag{3.18}$$

where δ_n^+ and δ_n^- are the sets of element nodes that are on the subdomains where $f > 0$ and $f < 0$, respectively. We assume here that the discontinuous function $\Phi^{(r)}$ is as sufficiently smooth as to be interpolated exactly by standard shape functions. Thus, $\Phi^{(r)+}$ and $\Phi^{(r)-}$ can be described in terms of standard shape functions by

$$\begin{aligned} \Phi^{(r)+}(\mathbf{X}) &= \sum_{I=1}^{n_e} N_I(\mathbf{X})\Phi^{(r)+}(\mathbf{X}_I) \\ \Phi^{(r)-}(\mathbf{X}) &= \sum_{I=1}^{n_e} N_I(\mathbf{X})\Phi^{(r)-}(\mathbf{X}_I) \end{aligned} \tag{3.19}$$

Substituting Equations (3.17) and (3.18) into (3.19), we will have

$$\begin{aligned} \sum_{I\in\delta_n^-} N_I(\mathbf{X})[\![\Phi^{(r)}]\!]_{\mathbf{X}=\mathbf{X}_I} &= \sum_{J\in\delta^r} \Psi_J^{r+}(\mathbf{X}) \times \mathrm{mes}(\Omega^e)\frac{r}{n_{\mathrm{SD}}}[\![\nabla\Phi_{,r}^{(r)}.\mathbf{e}_J^{\mathrm{c}}]\!]_J \\ \sum_{I\in\delta_n^+} -N_I(\mathbf{X})[\![\Phi^{(r)}]\!]_{\mathbf{X}=\mathbf{X}_I} &= \sum_{J\in\delta^r} \Psi_J^{r-}(\mathbf{X}) \times \mathrm{mes}(\Omega^e)\frac{r}{n_{\mathrm{SD}}}[\![\nabla\Phi_{,r}^{(r)}.\mathbf{e}_J^{\mathrm{c}}]\!]_J \end{aligned} \tag{3.20}$$

The Equation (3.20) is the general formulation to derive the enrichment functions using non-nodal enrichment points for a discontinuity in the rth derivative of the field. For example, 2D enrichment functions given in equation (3.11) can be obtained from Equation (3.20) by assigning $r = 1$ which gives $\Phi^1(\mathbf{X}) = H(f(\mathbf{X})) \times f(\mathbf{X})$.

Chapter 4

Governing Equations, Weak Formulation and Discretization

4.1 governing equations

Considering dynamic form of a two-dimensional problem, the governing equation is

$$\frac{\partial P_{ji}}{\partial X_j} + \rho_0 b_i - \rho_0 \ddot{u}_i = 0 \quad in \quad \Omega_0 \tag{4.1}$$

where $\mathbf{P}$ is the nominal stress tensor, ρ_0 is the initial density and $\mathbf{b}$ is the body force vector per unit mass. The boundary conditions are

$$\begin{aligned} u_i &= \bar{u}_i && \text{on} \quad \Gamma^0_{\mathrm{u}} \\ [\![u]\!]_i &= [\![\bar{u}]\!]_i && \text{on} \quad \Gamma^0_{\mathrm{uc}} \\ n^0_j P_{ji} &= \bar{t}^0_i && \text{on} \quad \Gamma^0_{\mathrm{t}} \\ n^{0\pm}_j P^{0\pm}_{ji} &= \tau^{0\mathrm{c}}_i([\![u]\!]_i) && \text{on} \quad \Gamma^0_{\mathrm{c}} \end{aligned} \tag{4.2}$$

where $\bar{\mathbf{u}}$ is the applied displacement on the Dirichlet boundary Γ^0_{u} and $[\![\bar{\mathbf{u}}]\!]$ is the prescribed displacement jump on a set of non-nodal enrichment parameters Γ^0_{uc}, $\bar{\mathbf{t}}^0$ is the applied traction on the Neumann boundary Γ^0_{t}, $\mathbf{n}$ is the outward normal to the designated boundaries and $\tau^{0\mathrm{c}}$ is the cohesive traction across the crack boundary Γ^0_{c}. Superscripts plus and minus signs indicate the positive and negative value of the level set function f, respectively. Indicial notation is used for lower case indices.

It must be stressed out that a crack tip can be simply modeled by imposing a prescribed displacement jump equal to zero at crack tip point as

$$[\![u]\!]_i = 0 \quad \text{at crack tip} \tag{4.3}$$

4.2 WEAK FORMULATION

The admissible space for the trial and test functions are defined as follows:

$$\begin{aligned}\mho &= \{\mathbf{u} \,|\, \mathbf{u} \in \mathrm{C}^0,\, \mathbf{u} = \bar{\mathbf{u}} \text{ on } \Gamma_{\mathrm{u}}^0,\, [\![\mathbf{u}]\!] = [\![\bar{\mathbf{u}}]\!] \text{ on } \Gamma_{\mathrm{uc}}^0,\, \mathbf{u} \text{ discontiniuous on } \Gamma_{\mathrm{c}}\} \\ \mho_0 &= \{\delta\mathbf{u} \,|\, \delta\mathbf{u} \in \mathrm{C}^0,\, \delta\mathbf{u} = 0 \text{ on } \Gamma_{\mathrm{u}}^0,\, [\![\delta\mathbf{u}]\!] = 0 \text{ on } \Gamma_{\mathrm{uc}}^0,\, \delta\mathbf{u} \text{ discontiniuous on } \Gamma_{\mathrm{c}}\}\end{aligned} \tag{4.4}$$

The weak form is expressed as an integral form of the momentum equation so that for $\mathbf{u} \in \mho$ and $\forall\, \delta\mathbf{u} \in \mho_0$

$$\delta W^{\mathrm{kin}} = \delta W^{\mathrm{ext}} - \delta W^{\mathrm{int}} + \delta W^{\mathrm{coh}} \tag{4.5}$$

where δW^{kin} is the kinetic work, δW^{ext} is the external work, δW^{int} is the internal work and δW^{coh} is the cohesive work achieved by the cohesive traction on the crack surface. So, the Equation (4.5) can be expanded as follows

$$\int_{\Omega_0} \delta\mathbf{u}.\rho_0\ddot{\mathbf{u}}\mathrm{d}\Omega_0 = \int_{\Omega_0} \delta\mathbf{u}.\rho_0\mathbf{b}\mathrm{d}\Omega_0 + \int_{\Gamma_{\mathrm{t}}^0} \delta\mathbf{u}.\bar{\mathbf{t}}^0\mathrm{d}\Gamma_0 - \int_{\Gamma_{\mathrm{c}}} [\![\delta\mathbf{u}]\!].\boldsymbol{\tau}^{\mathrm{c}}\mathrm{d}\Gamma_0 - \int_{\Omega_0} \frac{\partial\delta\mathbf{u}}{\partial\mathbf{X}} : \mathbf{P}\mathrm{d}\Omega_0 \tag{4.6}$$

where $[\![\delta\mathbf{u}]\!]$ and $\boldsymbol{\tau}$ are the variation of displacement jump and cohesive traction applied on the discontinuity surface, respectively.

4.3 DISCRETIZATION

The finite element discretization relates each of the virtual work terms in Equation (4.5) to an associated nodal force as follows:

$$\mathbf{f}^{\mathrm{kin}} = \mathbf{f}^{\mathrm{ext}} - \mathbf{f}^{\mathrm{int}} + \mathbf{f}^{\mathrm{coh}} \tag{4.7}$$

where $\mathbf{f}^{\mathrm{kin}}$, $\mathbf{f}^{\mathrm{ext}}$, $\mathbf{f}^{\mathrm{int}}$ and $\mathbf{f}^{\mathrm{coh}}$ are the kinematic, external, internal and cohesive forces, respectively. These forces are constructed by assembling the local element force vectors:

$$\mathbf{f}_e^{\mathrm{kin}} = \int_{\Omega^e} \rho\mathbf{N}_e^{g\mathrm{T}}\mathbf{N}_e^g\mathrm{d}\Omega^e\ddot{\mathbf{d}}_e^g \tag{4.8}$$

$$\mathbf{f}_e^{\text{ext}} = \int_{\Omega^e} \rho \mathbf{N}_e^{\mathrm{T}} \mathbf{b}_e \mathrm{d}\Omega^e + \int_{\Gamma_{\mathrm{t}}^e} \mathbf{N}_e^{\mathrm{T}} \bar{\mathbf{t}} \mathrm{d}\Gamma_{\mathrm{t}}^e \tag{4.9}$$

$$\mathbf{f}_e^{\text{int}} = \int_{\Omega^e} \mathbf{B}_e^{g\mathrm{T}} \mathbf{S}_e^g \mathrm{d}\Omega^e \tag{4.10}$$

$$\mathbf{f}_e^{\text{coh}} = -\int_{\Gamma_{\mathrm{c}}^e} [\![\boldsymbol{\Psi}]\!]^{\mathrm{T}} \boldsymbol{\tau}^{\mathrm{c}} \mathbf{n} \mathrm{d}\Gamma_{\mathrm{c}}^e \tag{4.11}$$

Here the superscript e is the element number, $\mathbf{S}$ is the second Piola-Kirchhoff stress in Voigt form, $\mathbf{d}_e^g = [u_e, [\![u]\!]_J]$ is the generalized nodal coefficient matrix consisting of the nodal displacements and the enrichment parameters, $\mathbf{N}_e^g$ is the union of regular shape functions and enrichment functions and $\mathbf{B}_e^g$ is generalized strain-displacement matrix. The $\mathbf{N}_e^g$ matrix is given by

$$\mathbf{N}_e^g = [\mathbf{N}_e^0, \boldsymbol{\Psi}_J] \tag{4.12}$$

The $\mathbf{B}_e^g$ is also given by

$$\mathbf{B}_e^g = [\mathbf{B}_e^0, \mathbf{B}_e^{\mathrm{c}}] \tag{4.13}$$

where

$$\mathbf{B}_I^0 = \begin{bmatrix} N_{I,\mathrm{X}}\, x_{,\mathrm{X}} & N_{I,\mathrm{X}}\, y_{,\mathrm{X}} \\ N_{I,\mathrm{Y}}\, x_{,\mathrm{Y}} & N_{I,\mathrm{Y}}\, y_{,\mathrm{Y}} \\ N_{I,\mathrm{X}}\, x_{,\mathrm{Y}} + N_{I,\mathrm{Y}}\, x_{,\mathrm{X}} & N_{I,\mathrm{X}}\, y_{,\mathrm{Y}} + N_{I,\mathrm{Y}}\, y_{,\mathrm{X}} \end{bmatrix} \tag{4.14}$$

$$\mathbf{B}_I^{\mathrm{c}} = \begin{bmatrix} \Psi_{I,\mathrm{X}}\, x_{,\mathrm{X}} & \Psi_{I,\mathrm{X}}\, y_{,\mathrm{X}} \\ \Psi_{I,\mathrm{Y}}\, x_{,\mathrm{Y}} & \Psi_{I,\mathrm{Y}}\, y_{,\mathrm{Y}} \\ \Psi_{I,\mathrm{X}}\, x_{,\mathrm{Y}} + \Psi_{I,\mathrm{Y}}\, x_{,\mathrm{X}} & \Psi_{I,\mathrm{X}}\, y_{,\mathrm{Y}} + \Psi_{I,\mathrm{Y}}\, y_{,\mathrm{X}} \end{bmatrix} \tag{4.15}$$

where $(.)_{,i}$ indicates the partial derivative along ith coordinate direction.

4.4 COHESIVE LAW

The cohesive model is applied to the damage evolution created by the crack. In a cohesive model, a surface traction determined by a cohesive law is applied onto the crack surfaces Γ_{c} such that the energy dissipated due to the crack evolution matches

the critical fracture energy. In this study, we considered only the normal component of the traction. The normal displacement jump δ_N is defined by

$$\delta_N = \mathbf{n}.[\![\mathbf{u}]\!] = \mathbf{n}.\sum_{J\in\delta_{\text{en}}} [\![\Psi]\!]_J [\![\mathbf{u}]\!]_J \tag{4.16}$$

In general, the cohesive traction can be computed incrementally with radial return algorithm as follows:

$$\begin{aligned}
&\textbf{input}: \ \delta_N \\
&\delta_N^0 = \delta_N^{\text{prev}} \\
&\tau_N^0 = \tau_N^{\text{prev}} \\
&E^0 = E^{\text{prev}} \\
&\textbf{for } i = 1 \text{ to } N \\
&\quad \delta_N^i = \delta_N^{i-1} + \frac{i \times \ \delta_N}{N} \\
&\quad \textbf{if } \delta_N^i > 0 \\
&\qquad \tau_N^{\text{trial}} = \tau_N^{i-1} + E^{i-1}(\delta_N^i - \delta_N^{i-1}) \\
&\qquad \textbf{if } \tau_N^{\text{trial}} > f(\delta_N^i) \\
&\qquad\quad \tau_N^i = f(\delta_N^i) \\
&\qquad\quad E^i = \tau_N^i / \delta_N^i \\
&\textbf{return } \tau_N^i
\end{aligned} \tag{4.17}$$

where δ_N and δ_N^i are the normal displacement and incremental displacement, respectively. In the radial return algorithm, the loop invariant is $E_N = \tau_N^i/\delta_N^i$ while δ_N^i and τ_N^i are underneath the traction law illustrated in Figure 4.1. Thus, for the linear cohesive model, we have

$$\delta_{\max} = \frac{2G_F}{\tau_{\max}} \tag{4.18}$$

4.5 NUMERICAL INTEGRATION

For computation of the integral Equations (4.8) -(4.10) in an enriched element where the integrands are discontinuous, a modified numerical quadrature scheme such as

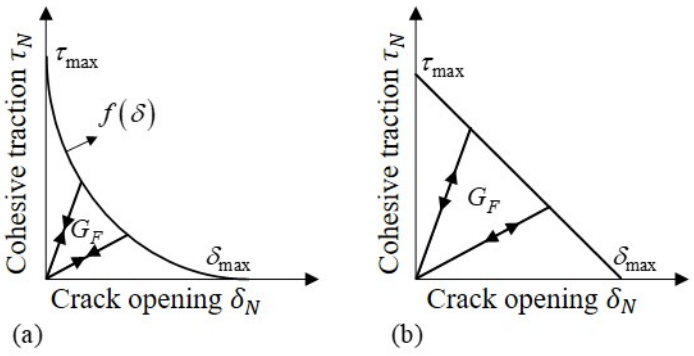

Figure 4.1 Cohesive law; the area under the cohesive law curve is the same as the fracture energy (a) a general cohesive law; and (b) a linear cohesive law.

subdomain integration is needed. In subdomain integration, the element domain is partitioned into several subdomains where the Gauss points are positioned as shown in Figure 4.2(b)-(c). Here we adopt two different subdomain integration schemes depending on the parent domains where the enrichment functions are defined. For the Duffy's parent domain, the enrichment functions are given in Equation (2.9) and the straight discontinuity shown in Figure 4.2(a) is mapped to a high curvature interface shown in Figure 4.2(b). To maintain the accuracy of the integration, the interface is discretized, which leads to increased number of subdomains. For the standard parent domain shown in Figure 4.2(c), the enrichment functions are given in Equation (2.11). Since these enrichment functions are non-polynomial functions, higher number of Gauss points is required to maintain the integration accuracy.

4.6 Time integration scheme and critical time step

The explicit time integration was used over the whole domain. The explicit time integration is conditionally stable, i.e. it is stable when

$$\Delta t \leq \Delta t_{\mathrm{c}} = \frac{2}{\omega_{\max}} \tag{4.19}$$

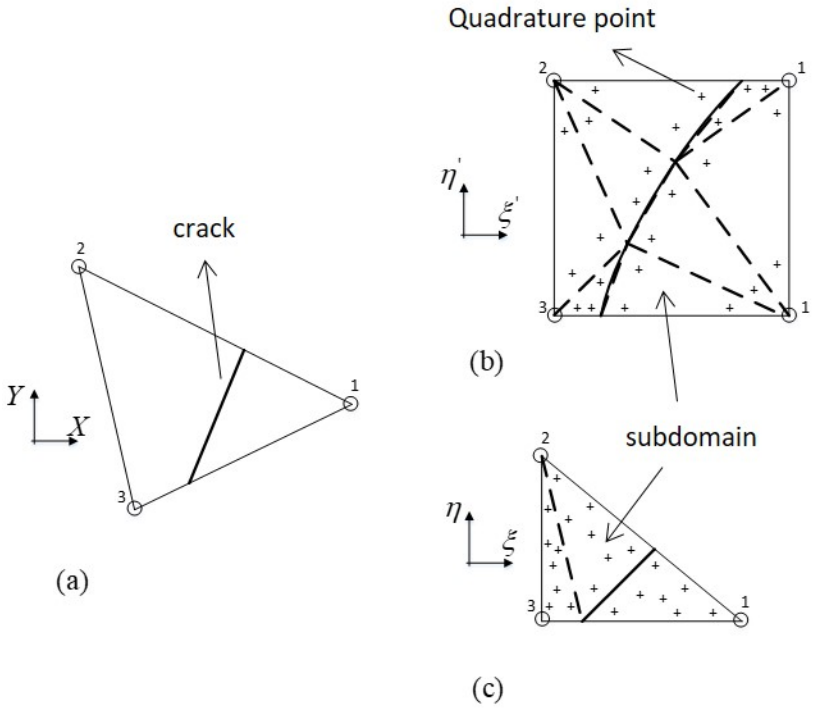

Figure 4.2 numerical integration with the subdomain integration schemes; (a) a cracked element in physical coordinates; (b) Duffy's parent domain; and (c) regular parent coordinates.

By studying the frequencies ω_i of the one-dimensional discrete system $\omega_i^2 \mathbf{M}\mathbf{d}_i = \mathbf{K}\mathbf{d}_i$, the variation of the critical time step according to the normalized location of the crack was determined. Figure 4.3 compares the normalized critical time step of standard XFEM with non-nodal XFEM. The critical time steps are normalized with respect to $\Delta_c^0 = l/c$.

For standard XFEM, the peak value of the critical time step occurs when the crack is in the middle of the element while for non-nodal XFEM, the minimum of the critical time step occurs at the middle. This implies that the non-nodal XFEM is more efficient than the standard XFEM. Furthermore, for standard XFEM, the critical time step drops linearly to zero as the crack location approaches to the element nodes

which leads to numerical difficulties in explicit time integration schemes. However, since non-nodal XFEM has no zero critical time step, it can be directly used in explicit methods.

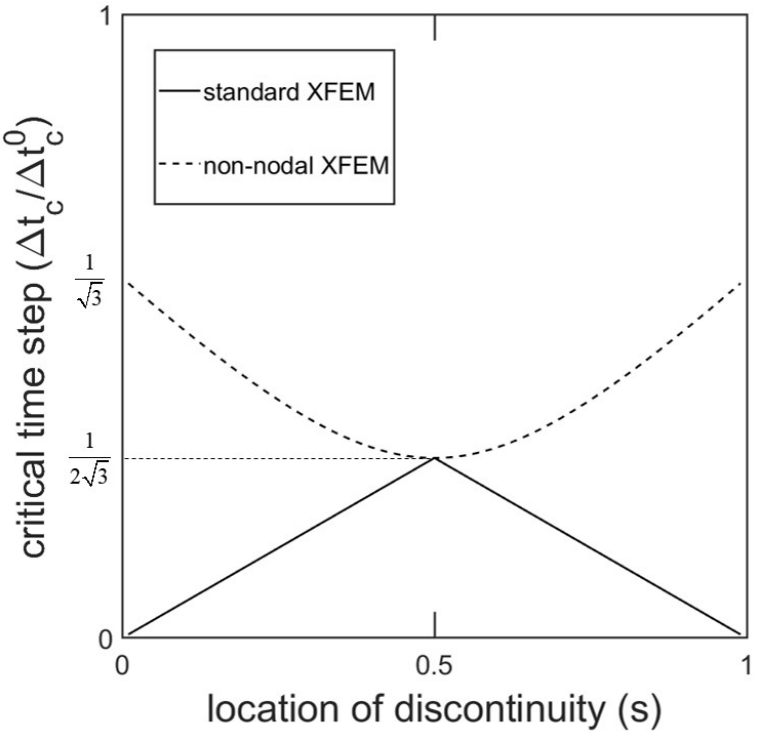

Figure 4.3 The variation of normalized critical time step size according to the normalized location of the discontinuity.

Chapter 5

Numerical Examples

In the first two examples, the convergence of the proposed method is validated through static problems from linear elastic fracture mechanics. To verify the method for modeling dynamic crack propagation, we consider crack propagation for three benchmark problems whose experimental results are available. To effectively demonstrate the benefits of the method, we solve the problems using three approaches: (i) a standard XFEM, (ii) a non-nodal XFEM considering only strong enrichment functions Ψ^{u}, and (iii) the linear complete non-nodal XFEM. The numerical solutions are compared with experimental data. The central difference method for time integration is used with a Courant number of 0.1. All simulations are solved using constant strain triangular elements, plane strains and thicknesses of unity. The fracture criterion was the maximum tensile stress computed at the crack front. The direction of the crack was selected to be the normal to the maximum tensile stress direction. To eliminate the awkward oscillations in stress computation, once an element failed, the stresses about the crack edge were averaged using nodal smoothing techniques.

The relative errors in the energy norm denoted by $R.E_{\mathrm{en}}$ and L^2-norm denoted by $R.E_{\mathrm{d}}$ used in the analysis are defined as

$$\left(R.E_{\mathrm{en}}\right)^2 = \frac{\int_\Omega (\boldsymbol{\varepsilon} - \boldsymbol{\varepsilon}^{\mathrm{h}})^{\mathrm{T}} \mathbf{C} (\boldsymbol{\varepsilon} - \boldsymbol{\varepsilon}^{\mathrm{h}}) \, \mathrm{d}\Omega}{\int_\Omega \boldsymbol{\varepsilon}^{\mathrm{T}} \mathbf{C} \boldsymbol{\varepsilon} \, \mathrm{d}\Omega}, \tag{5.1a}$$

$$\left(R.E_{\mathrm{d}}\right)^2 = \frac{\int_\Omega (\mathbf{u} - \mathbf{u}^{\mathrm{h}})^2 \, \mathrm{d}\Omega}{\int_\Omega \mathbf{u}^2 \, \mathrm{d}\Omega}. \tag{5.1b}$$

5.1 Near-tip crack field

To demonstrate the capability of the proposed method for reproducing non-smooth solutions, a square patch with the same length and height $L = H = 2$ and a crack length $H/2 = 1$ is considered as shown in Figure 5.1. Tractions are prescribed along

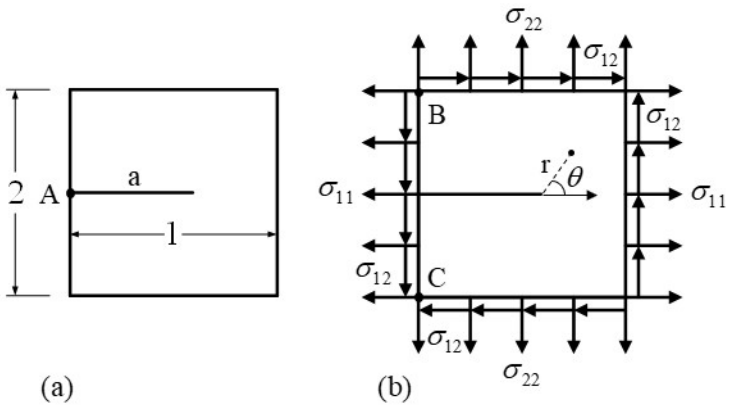

Figure 5.1 A square patch for the near-tip crack problem: (a) geometry; and (b) boundary conditions.

the boundary and the rigid body motions are avoided by prescribing displacements at nodes B and C shown in Figure 5.1(b). The closed-form stress fields ahead of a crack tip for the mode I in polar coordinates (r, θ) are given by

$$\sigma_{11}(r,\theta) = \frac{K_I}{\sqrt{2\pi r}} \cos\frac{\theta}{2}\left(1 - \sin\frac{\theta}{2}\sin\frac{3\theta}{2}\right), \tag{5.2a}$$

$$\sigma_{22}(r,\theta) = \frac{K_I}{\sqrt{2\pi r}} \cos\frac{\theta}{2}\left(1 + \sin\frac{\theta}{2}\sin\frac{3\theta}{2}\right), \tag{5.2b}$$

$$\sigma_{12}(r,\theta) = \frac{K_I}{\sqrt{2\pi r}} \cos\frac{\theta}{2}\sin\frac{\theta}{2}\cos\frac{3\theta}{2}. \tag{5.2c}$$

The closed-form displacements are also given by

$$u_1(r,\theta) = \frac{K_I}{2\mu}\sqrt{\frac{r}{2\pi}} \cos\frac{\theta}{2}\left(k - 1 + 2\sin^2\frac{\theta}{2}\right), \tag{5.3a}$$

$$u_2(r,\theta) = \frac{K_I}{2\mu}\sqrt{\frac{r}{2\pi}} \sin\frac{\theta}{2}\left(k + 1 - 2\cos^2\frac{\theta}{2}\right) \tag{5.3b}$$

where μ is the shear modulus and k is the Kolosov constant defined as

$$k = \begin{cases} 3 - 4\,\nu & \text{(plane strain)}, \\ \dfrac{3-\nu}{1+\nu} & \text{(plane stress)}. \end{cases} \tag{5.4}$$

The material properties selected are: Young's modulus $E = 10^5$ and Poisson's ratio $\nu = 0.3$. The stress intensity factor is prescribed as $K_I = 1.0$.

A convergence study is carried out using structured linear triangular elements. Plots of errors in both energy norm and L^2-norm are provided in Figure 5.2. The rates of convergence in the energy norm for the regular FEM, the standard XFEM, and the proposed method are around 0.49 which is very close to the optimal value of 0.5. Notice that the convergence rate in the energy norm for non-smooth problems is less than unity; it is $O(h^{1/2})$ for the crack-tip problem as indicated in [4].

Also, the results demonstrate that the proposed method outperforms the standard XFEM as the graph shows a constant shift toward lower error. For the non-nodal XFEM with only Ψ^{u} enrichment, the convergence rate is sub-optimal but it increases with mesh refinement as it is illustrated from L^2-norm results in Figure 5.2(b).

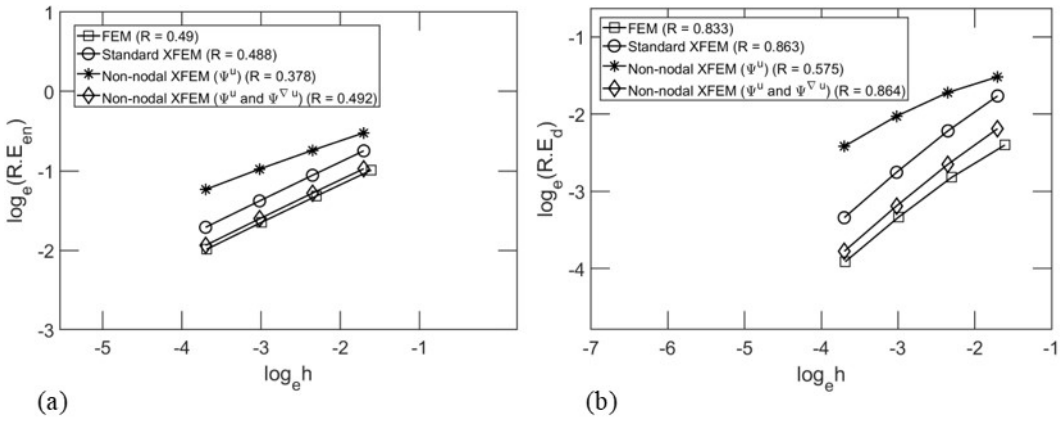

Figure 5.2 Rate of convergence for the near-tip crack field problem for several enrichment schemes: (a) Energy-norm errors; and (b) L^2-norm errors.

One advantage of the proposed method is to improve accuracy by imposing Dirichlet boundary conditions on the interface. In doing so, closed-form displacement jumps are imposed at the non-nodal point on the left edge, i.e., point A in Figure 5.1. These constraints can be expressed as

$$[\![\bar{u}_A]\!]_X = 0, \qquad [\![\bar{u}_A]\!]_Y = -2\,u_2(1,\pi).$$

A contour plot of the Mises stress and the convergence results on L^2-norm are displayed in Figure 5.3. The graph shows that a simple Dirichlet boundary condition on the the interface shifts the results toward lower error for both non-nodal XFEM schemes. Also, this boundary condition leads to a slightly better convergence rates for the proposed method.

The stresses are compared with exact solutions using both an 80×80 struc-

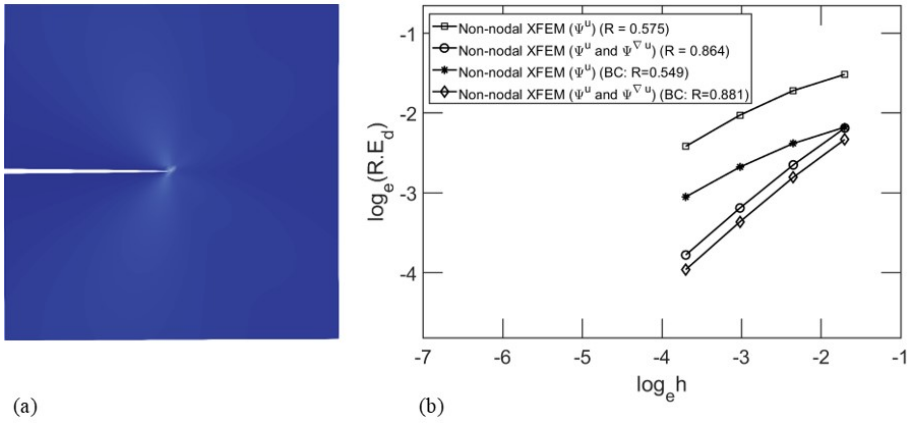

Figure 5.3 Comparison of rates of convergence of the near-tip crack field problem for non-nodal XFEM with and without Dirichlet boundary condition on the interface: (a) contour plot of Mises stress in deformed configuration ($\times$1000); and (b) L^2-norm errors.

tured mesh and an irregular mesh which is fine around the crack tip as shown in Figure 5.4(a)-(b). The stresses computed along $\theta = 0$ from the crack tip are shown in Figure 5.5(a)-(c) (respectively, 5.6) and the angular variation of stresses at $r = 0.1$a

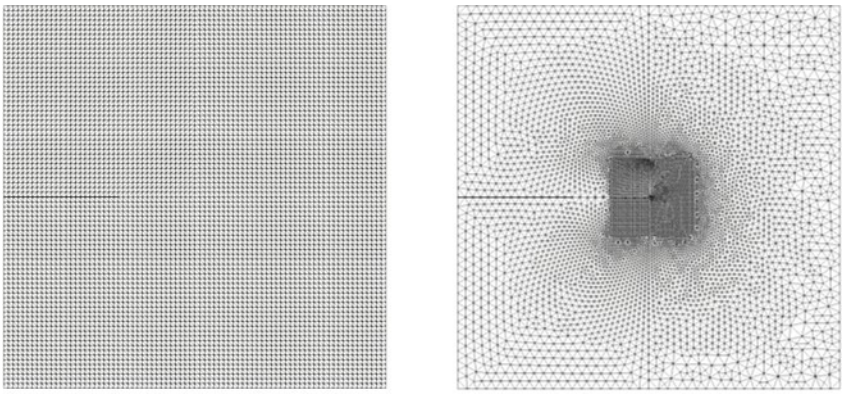

Figure 5.4 Mesh used for the stress convergence of the near-tip crack problem: (a) an 80×80 structured mesh; and (b) an irregular mesh of around 13000 elements.

from the crack edge are shown in Figure 5.5(d)-(e) (resp. 5.6). As it can be seen, the stresses oscillate near the crack tip for both meshes. The singularity at crack-tip also has not been captured. This is expected because we have not introduced any enrichment functions to capture the near-tip singular fields. However, with mesh refinement, the computed stresses converge to the closed-form solutions.

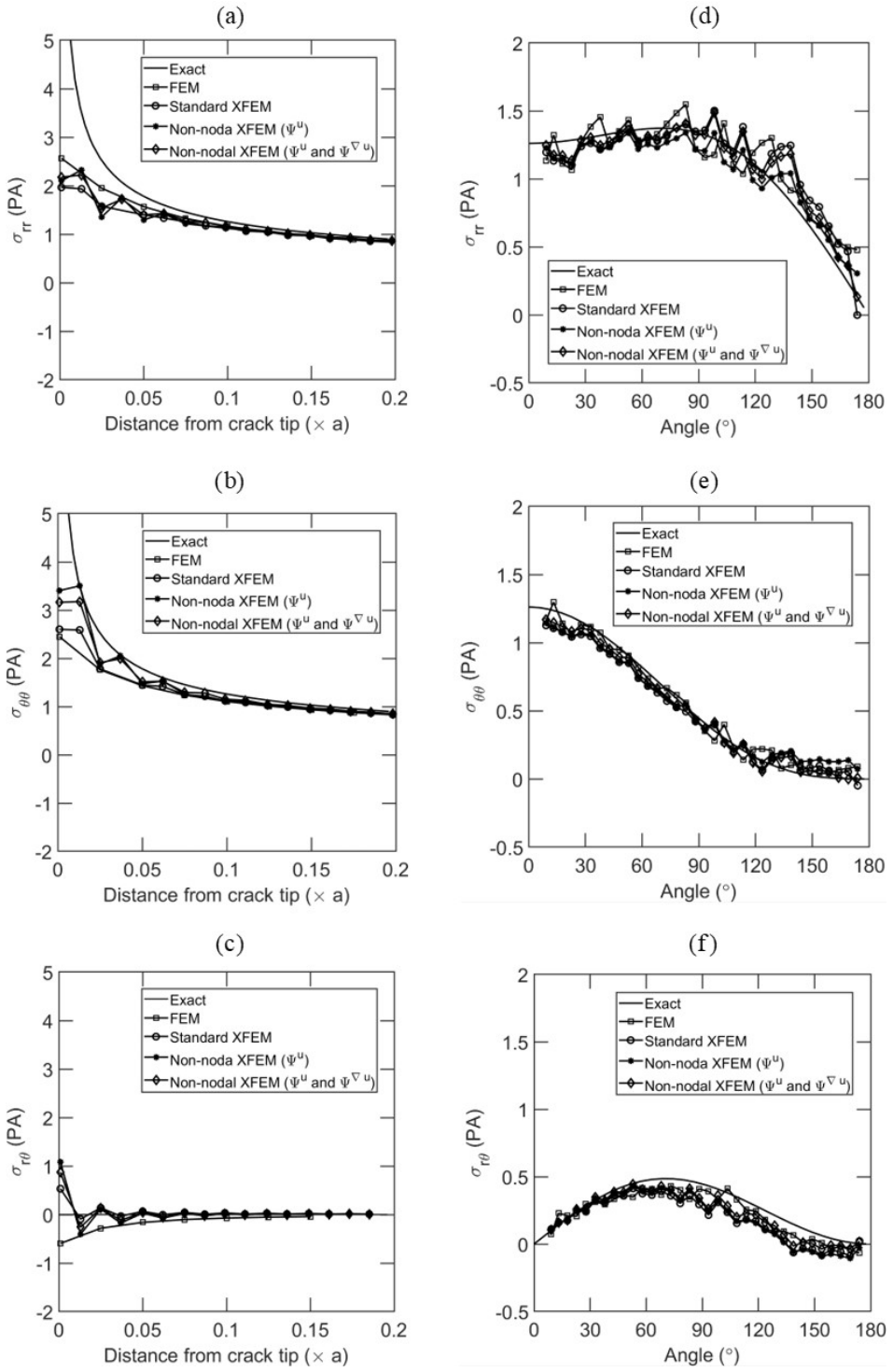

Figure 5.5 Stresses of the near-tip crack problem for the 80×80 structured mesh: (a-c) ahead of the crack tip; (d-f) angular variation along constant radius ($r = 0.1$a).

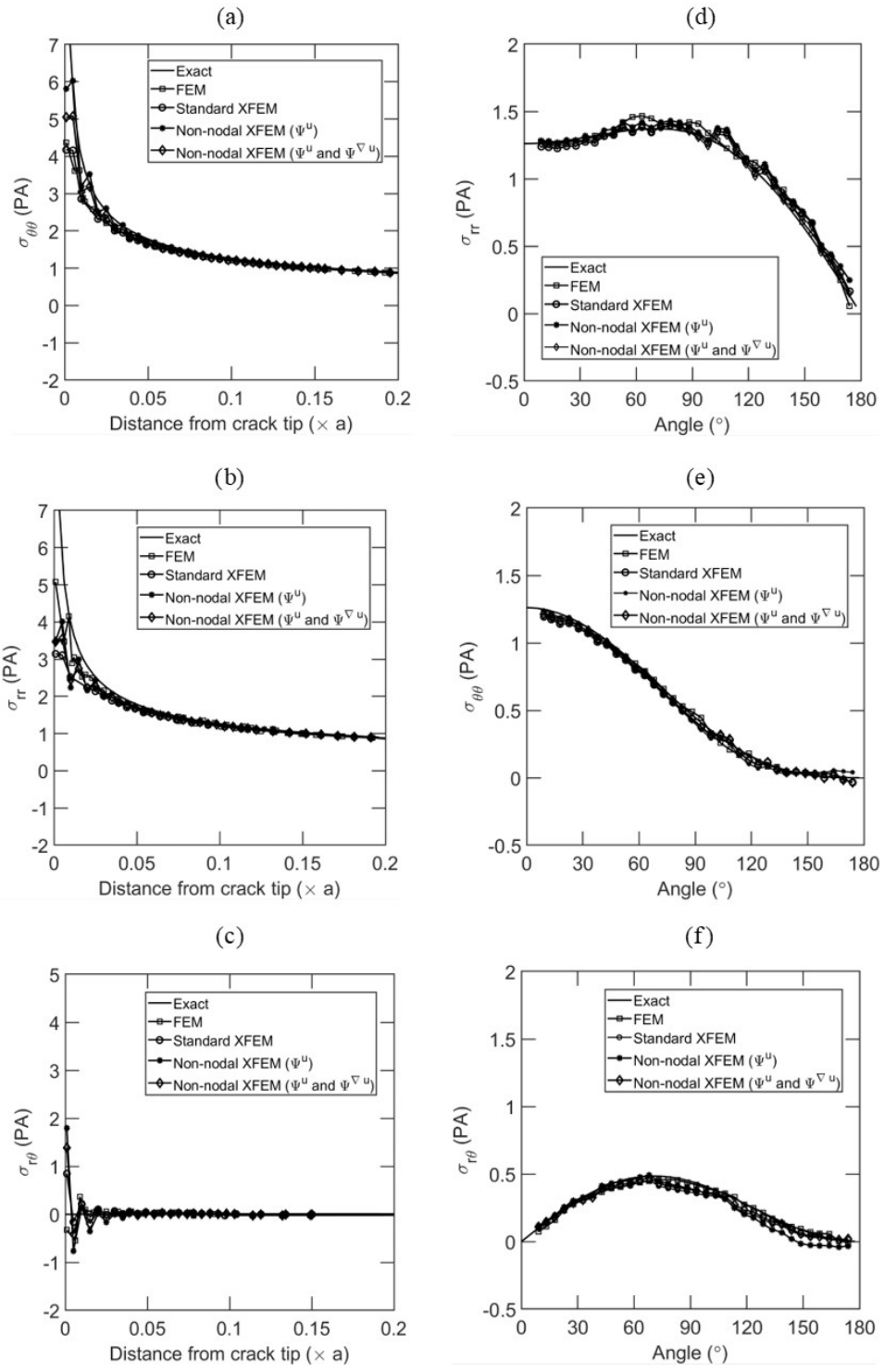

Figure 5.6 Stresses of the near-tip crack problem for irregular mesh: (a-c) ahead of the crack tip; (d-f) angular variation along constant radius ($r = 0.1$a).

5.2 Stress concentration in an infinite plate with a circular hole

To demonstrate the performance of the proposed method for modeling of discontinuities in strains, an infinite plate with a small circular hole of radius a subjected to uniform tension σ along X direction is considered (see Figure 5.7(a)). Since the exact solution is given for the region close to the circle [21], we consider a square domain of edge length $2b$ with the circular hole at its center as in [31]. To take advantage of symmetry, only the upper right quadrant is considered as shown in Figure 5.7(b). The symmetric constraints are imposed on bottom and left edges; the exact tractions are imposed on top and right edges. The closed-form solutions for the stress distribution in polar coordinates (r, θ) are given by

$$\sigma_{11}(r,\theta) = \sigma\left[1 - \frac{a^2}{r^2}\left(\frac{3}{2}\cos 2\theta + \cos 4\theta\right) + \frac{3}{2}\frac{a^4}{r^4}\cos 4\theta\right],$$
$$\sigma_{22}(r,\theta) = \sigma\left[-\frac{a^2}{r^2}\left(\frac{1}{2}\cos 2\theta - \cos 4\theta\right) - \frac{3}{2}\frac{a^4}{r^4}\cos 4\theta\right],$$
$$\sigma_{12}(r,\theta) = \sigma\left[-\frac{a^2}{r^2}\left(\frac{1}{2}\sin 2\theta + \sin 4\theta\right) + \frac{3}{2}\frac{a^4}{r^4}\sin 4\theta\right].$$

The closed-form displacements are given by

$$u_1(r,\theta) = \frac{a\sigma}{8\mu}\left[\frac{r}{a}(k+1)\cos\theta + 2\frac{a}{r}((1+k)\cos\theta + \cos 3\theta) - 2\frac{a^3}{r^3}\cos 3\theta\right],$$
$$u_2(r,\theta) = \frac{a\sigma}{8\mu}\left[\frac{r}{a}(k-3)\sin\theta + 2\frac{a}{r}((1-k)\sin\theta + \sin 3\theta) - 2\frac{a^3}{r^3}\sin 3\theta\right].$$

We take Young's modulus $E = 10^5$ and Poisson's ratio $\nu = 0.3$. The analyses are performed considering the following parameters: $\sigma = 1$, $a = 0.3$, and $b = 1$. A convergence study is conducted using structured linear triangular elements in Figure 5.8.

The convergence rates were resulted slightly sub-optimal both for the standard XFEM and the proposed method; the proposed method obtains convergence rates of 0.9 and 1.813 in the energy norm and L^2-norm, respectively. However, the method with only strong enrichment function gives the convergence rates of 0.498 and

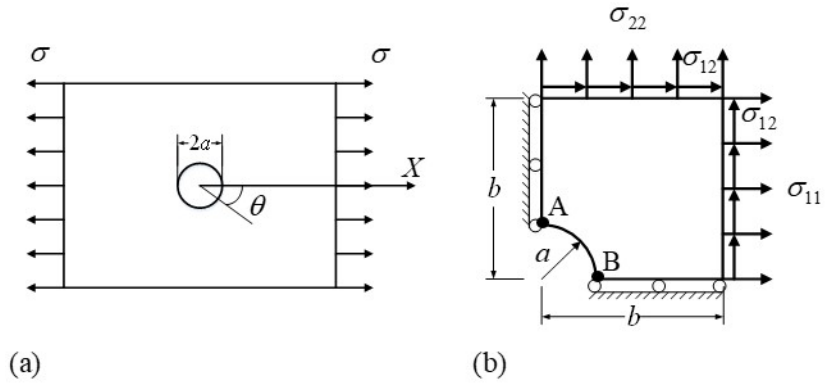

Figure 5.7 (a) Infinite plate with a circular hole subjected to uniform tension; and (b) upper right quadrant of a square of edge length $2b$ centered at $(0, 0)$ is modeled due to symmetry.

0.885. This is expected because the enrichment function Ψ^{u} can only capture strong discontinuities while there is a weak discontinuity inside elements in this problem.

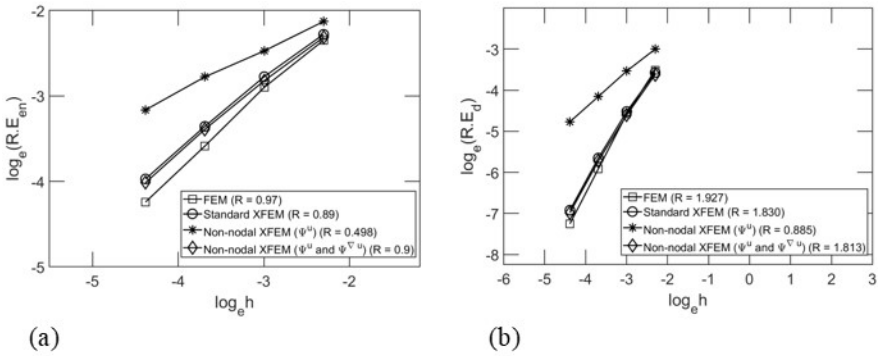

Figure 5.8 Rate of convergence for the plate with a hole in center problem for four enrichment schemes: (a) Energy-norm errors; and (b) $L2$-norm errors.

Contour plots for the normal stress σ_{11} are shown in Figure 5.9. Figure 5.9(a) shows that the maximum normal stress for both standard XFEM and the proposed method is 3.3 which is more than the theoretical value of 3.0. To improve the accuracy

of the results, two Dirichlet boundary conditions on left and bottom edges are imposed to the displacement jumps on the intersection points of the circular hole and square edges, i.e., points A and B in Figure 5.7. These constraints can be expressed as

$$[\![\bar{u}_A]\!]_X = 0, \qquad [\![\bar{u}_B]\!]_Y = 0$$

The resulted normal stresses are shown in Figure 5.9(b). As it can be seen, the maximum normal stress is 3.1, which is very closed to the theoretical value.

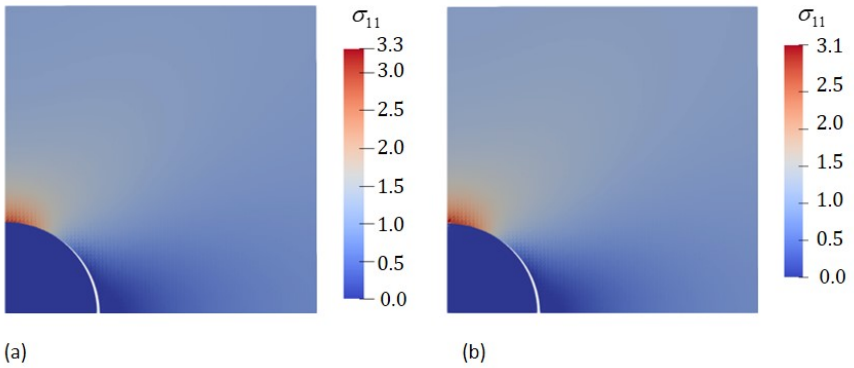

Figure 5.9 Contour plots of the normal stress σ_{11} in deformed configuration ($\times 1000$): (a) the proposed method and the standard XFEM; and (b) the proposed method with interface constrains.

5.3 EDGE-CRACKED PLATE UNDER IMPULSIVE LOADING

The first dynamic numerical example deals with an experiment carried out by Kalthoff and Winkler [19] in which a plate with two initial edge notches impacted by a projectile. Numerical results for this problem have been given by Belytschko et al. [8] and Song et al. [30]. Kalthoff observed two different failure modes by modifying the projectile speed V_0; at lower impact velocities, a brittle fracture with a crack propagation at an angle of about 70° was observed while at higher impact velocities, a strain localization, i.e. a shear band was observed at a negative angle of about -10°

with respect to the notch. In this work, we consider only the brittle fracture mode.

Due to twofold symmetry, only the upper half of the plate is modeled. A schematic description of the original problem and the upper part to be solved are shown in Figures 5.10(a)-(b), respectively. The symmetry condition $u_y = 0$ was imposed at the bottom edge of the model. The initial velocity is applied as a step function on the left edge on $0 \leq y \leq 25$mm. Assuming that the projectile and the plate have identical elastic impedance, an applied velocity of 16.5 m/s is chosen, which is one-half of the projectile speed in the experiment for the brittle fracture.

The plate is a maraging steel 18Ni1900 with the following material parameters: $\rho = 8000\,\mathrm{kg/m^3}$, $E = 190\,\mathrm{GPa}$ and $\nu = 0.3$; so, the Rayleigh wave speed is $c_R = 2799$m/s. The critical stress intensity factor is taken as $K_{Ic} = 68\mathrm{MPa}\sqrt{\mathrm{m}}$ which leads to a fracture energy $G_F = 2.217 \times 10^4 (J)/\mathrm{m}^2$. We used a linear cohesive crack model with a tensile strength of $\tau_{\max} = 844$MPa which corresponds to a critical crack opening displacement $\delta_{\max} = 5.245 \times 10^{-5}$m. To observe the mesh sensitivity, we have analyzed the model with three different uniform meshes: a 40×40 coarse mesh, a 80×80 medium mesh and a 120×120 fine mesh. The crack evolutions for each mesh are shown in Figures 5.11-5.13.

The finite element meshes and their crack growth trajectories are shown in Figure 5.14. The simulations terminated when the crack tip passed the upper boundary; all simulations yielded quite similar crack propagation trajectories which agree quite well with those obtained by the conventional XFEM [8, 30]. The numerical results for each simulation are listed in Table 5.1. The data in Table 5.1 shows that the crack begins to propagate at earlier times with mesh refinement, which leads to a shorter simulation time. For all simulations, the crack first grows primarily along an initial angle, then near the end of the simulation moves a little bit upward.

The initial and the overall crack propagation angles are increasing with mesh refinement; the overall angle is approaching to the experimental value with mesh re-

finement as the angle of 67.1° in fine mesh compares well with the experimental value of 70°.

The crack tip propagation speeds for 40×40 and 80×80 meshes resulted

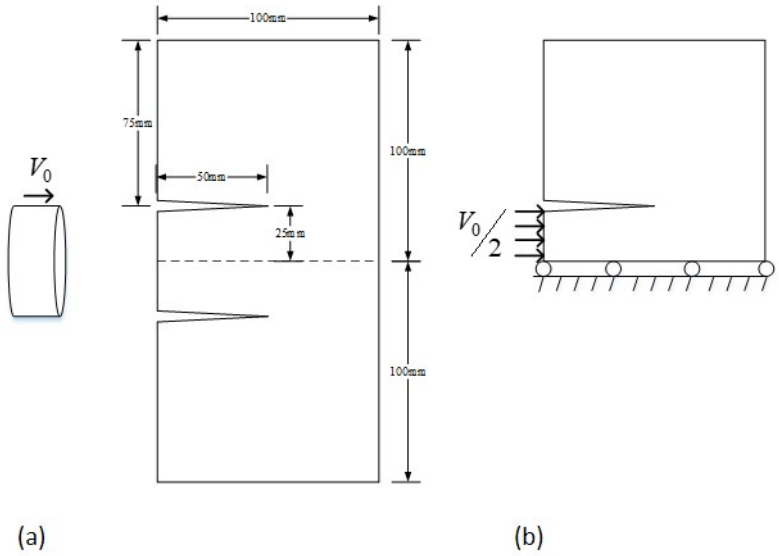

Figure 5.10 Experimental set-up and simulation model (a) Kalthoff experimental set-up for crack propagation under impulsive loading (b) Upper half of the plate used in the analysis.

Table 5.1 Crack propagation angles and timing data for the Kalthoff's experiment.

Mesh	Angles(°)		Time(μs)	
	Initial	Overall	Propagation	Simulation
40×40	60.16	62.45	25.61	81.28
80×80	61.87	64.74	25.59	79.98
120×120	63.34	67.1	19.79	77.4

by both the proposed method and the conventional XFEM are shown in Figure 5.15. As it is demonstrated in Figure 5.15(a), for both meshes, the proposed method yields very similar crack speeds. When the crack begins to propagate, its speed oscillates

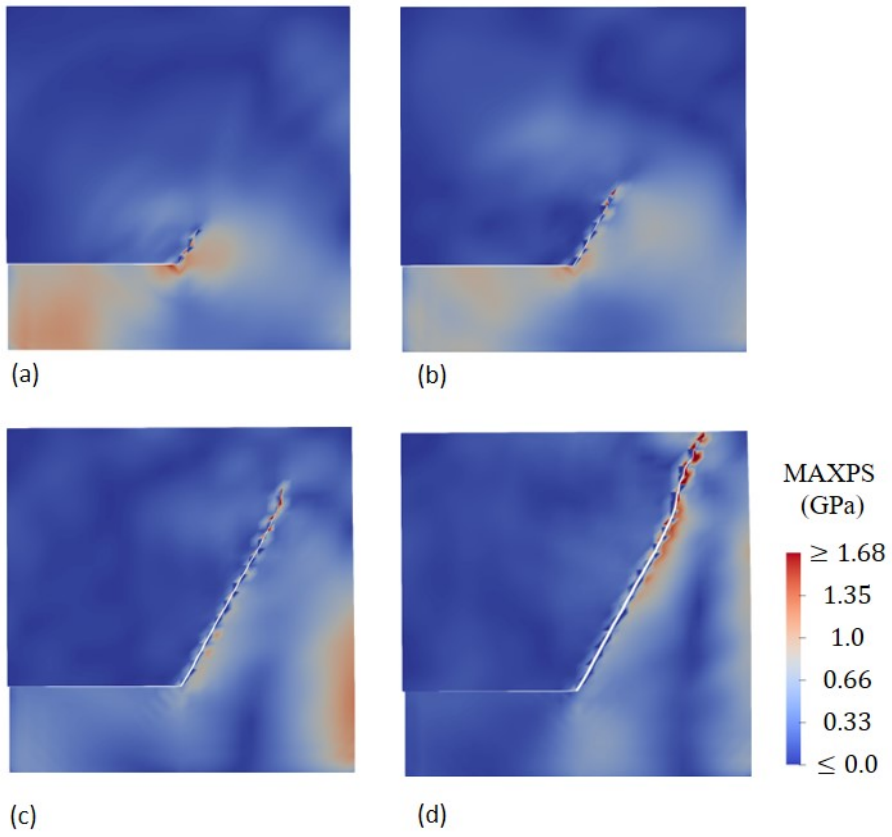

Figure 5.11 The computed crack paths on the 40×40 deformed mesh with a maximum principle stress at different time steps: (a) $t = 29.89\,\mu$s; (b) $t = 37.43\,\mu$s; (c) $t = 58.48\,\mu$s; and (d) $t = 81.28\,\mu$s.

around 2000 m/s and after 50 μs, the cracktip speed slowly decreases up to the end of the simulation. However, for the conventional XFEM, the crack speed for the fine mesh is significantly higher than for the coarse mesh. These results confirm the previous results in Reference [8]. Therefore, we can conclude that the proposed method demonstrates less mesh dependency than the conventional XFEM.

The examples above were also solved using linear complete non-nodal enrichment formulations. The crack evolutions for each mesh are shown in Figures 5.16-5.18. As demonstrated in Figure 5.19, similar to previous work, all simulations resulted similar crack paths. More details for each simulation are listed in Table 5.2.

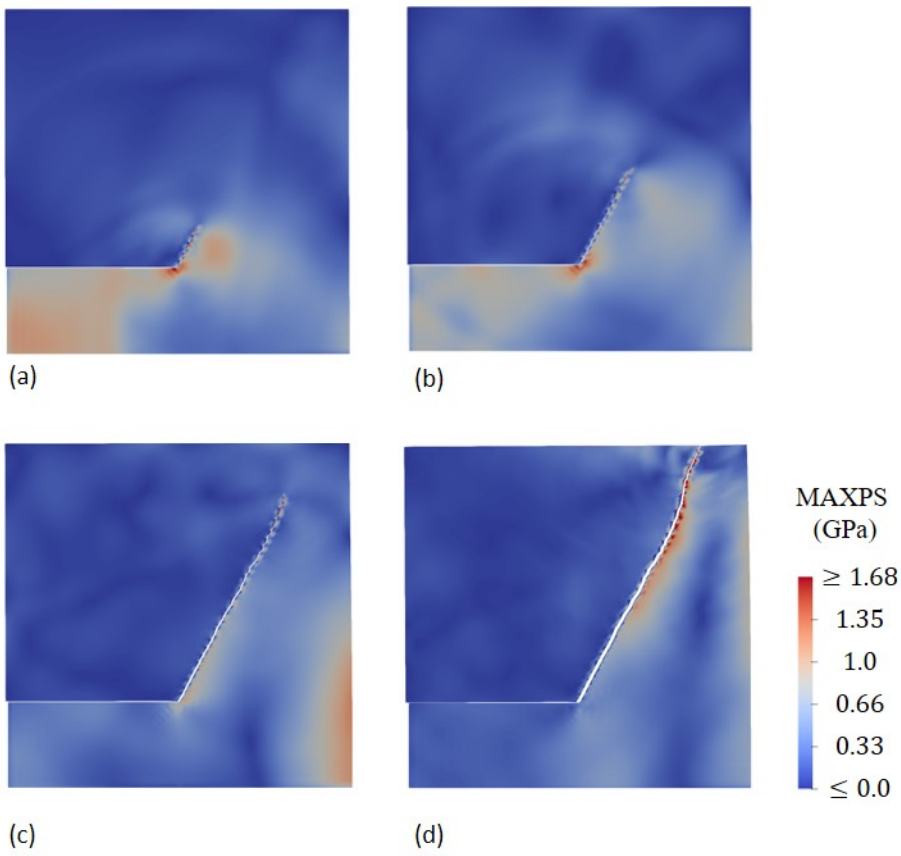

Figure 5.12 The computed crack paths on the 80×80 deformed mesh with a maximum principle stress at different time steps: (a) $t = 28.83\,\mu$s; (b) $t = 38.09\,\mu$s; (c) $t = 57.0\,\mu$s; and (d) $t = 79.98\,\mu$s.

The data in Table 5.2 shows that the overall crack propagation angle approaches to the experimentally obtained value of 70° degrees with mesh refinement. These angles are slightly bigger than the angles given by the Table 5.1. The difference may result from capturing the independent linear displacements in the presented work which yields to predict the strains more accurately.

The crack tip propagation speeds for 40×40 and 80×80 meshes are shown in Figure 5.20. For the linear complete enriched formulation, Figure 5.20(a) displays slightly bigger speed for 80×80 mesh than 40×40 mesh. For both meshes, when the crack begins to propagate, its speed increases up to 2000m/s and after $50\mu s$,

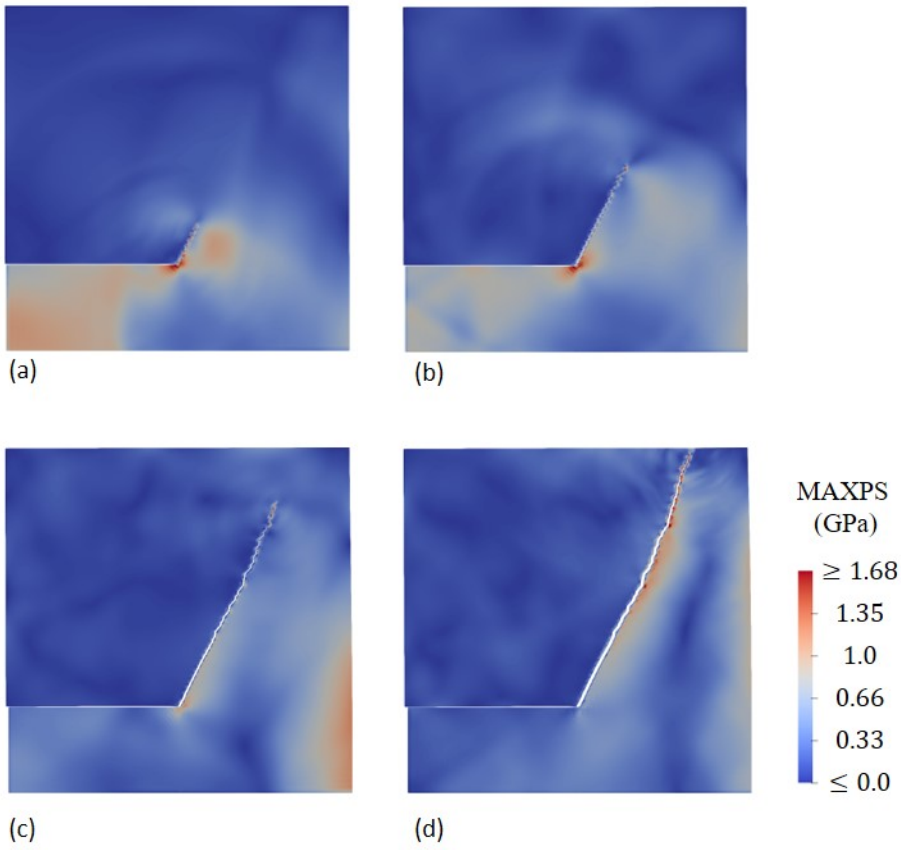

Figure 5.13 The computed crack paths on the 120×120 deformed mesh with a maximum principle stress at different time steps: (a) $t = 28.96\,\mu$s ; (b) $t = 38.45\,\mu$s; (c) $t = 56.49\,\mu$s; and (d) $t = 77.4\,\mu$s.

the cracktip speed decreases up to the end of the simulation. However, for the conventional XFEM result shown in Figure 5.20(b), there is a significant difference in the crack speeds for different meshes, which concludes that the proposed method demonstrates less mesh dependency than the conventional XFEM.

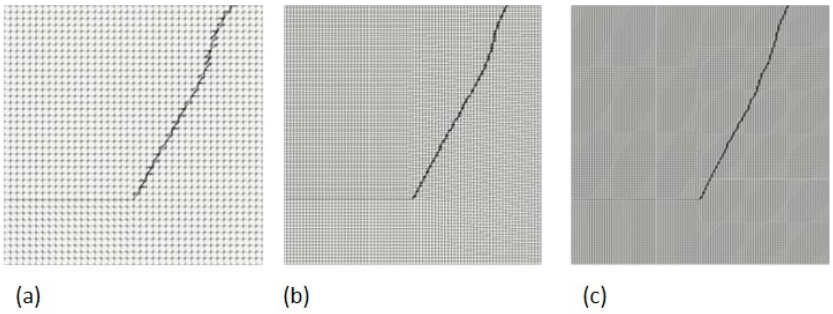

Figure 5.14 Comparison of crack propagation trajectories at final simulation step using triangular linear elements (a) 40×40 mesh; (b) 80×80 mesh; and (c) 120×120 mesh.

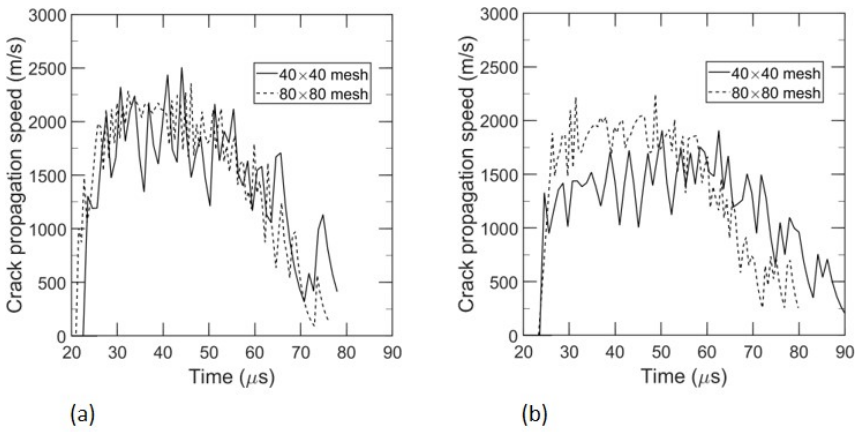

Figure 5.15 Crack speeds for the Kolthoff's experiment simulation: (a) the crack speed of this method and (b) the crack speed of the standard XFEM.

5.4 CRACK PATTERN IN THREE-POINT BENDING SPECIMENS WITH VARIABLE OFFSET NOTCH

Experiments concerning mixed mode dynamic crack propagation in three point bending specimens subjected to impact loading were conducted by John and Shah [18]. The numerical solutions for this example can be found in [30, 36, 28, 5, 6]. The exper-

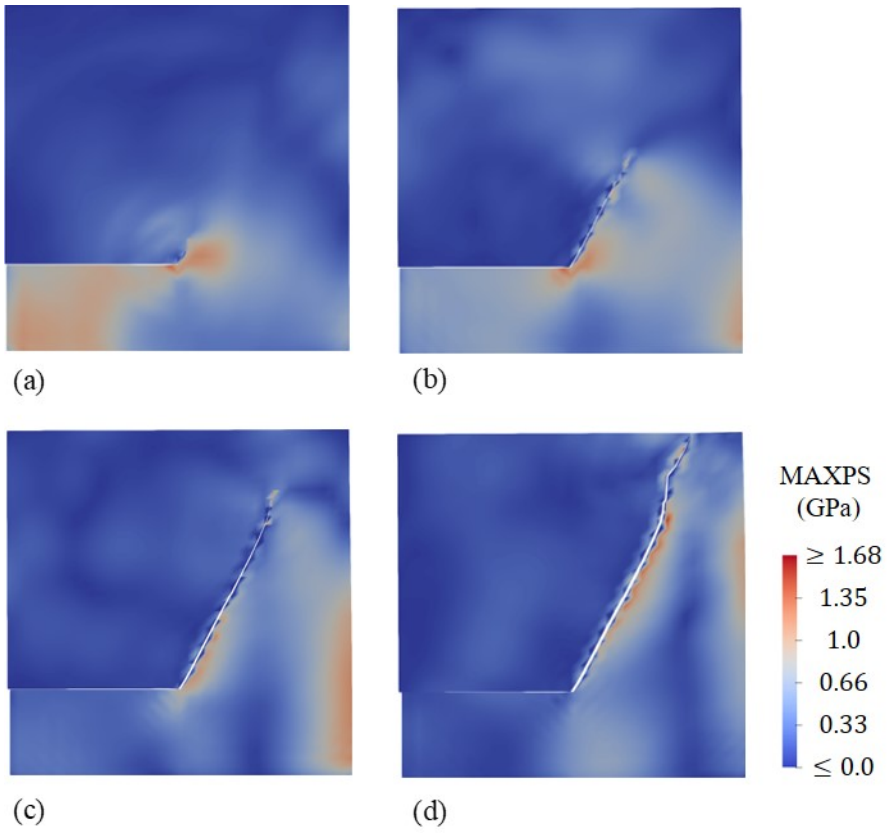

Figure 5.16 The computed crack paths using linear complete formulations on the 40×40 deformed mesh with a maximum principle stress at different time steps: (a) $t = 28.6\,\mu$s; (b) $t = 44.77\,\mu$s; (c) $t = 62.18\,\mu$s; and (d) $t = 84.55\,\mu$s.

imental setup is shown in Figure 5.21(a). To induce mixed-mode condition, a notch was located at a variable offset from the midspan. In these series of experiments, the crack patterns and crack initiation angles of specimens are examined for the offset notch at various locations. Finally, for several experiments, three crack propagation patterns were reported depending on the location of the notch which can be described by a normalized parameter γ.

$$\gamma = \frac{d_{\text{notch}}}{L/2} \tag{5.5}$$

where d_{notch} denotes the distance between the midspan and the notch, and L is the distance between the supports. A transition point was observed in the notch location

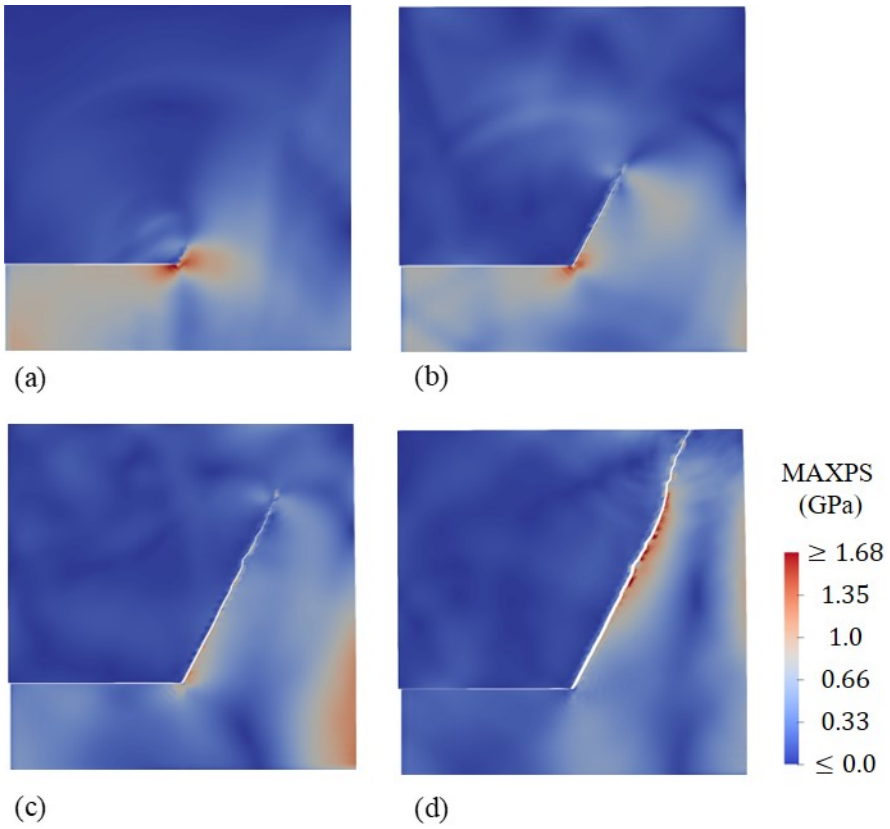

Figure 5.17 The computed crack paths using linear complete formulations on the 80×80 deformed mesh with a maximum principle stress at different time steps: (a) $t = 26.17\,\mu$s; (b) $t = 39.83\,\mu$s; (c) $t = 55.5\,\mu$s; and (d) $t = 81.32\,\mu$s.

γ_t, where failure changes from a crack growth at the offset notch ($\gamma < \gamma_t$) to a crack growth at the midspan ($\gamma > \gamma_t$). For a narrow transition region where offset parameter is close to γ_t, both notch and midspan crack initiate and propagate. The experimentally obtained value of γ_t is 0.77.

Material properties are given as density $\rho = 2400\,\text{kg/m}^3$, Young's modulus $E = 31.37\,\text{GPa}$, Poisson's ratio $\nu = 0.2$ and tensile strength of 10.45 MPa. A linear cohesive crack model was used with a fracture energy of $G_F = 19.58\,\text{J/m}^2$ and its corresponding critical crack opening displacement $\delta_{\max} = 3.75 \times 10^{-6}\,\text{m}$. To model the rubber pad between the beam and impact hammer, the velocity boundary condition

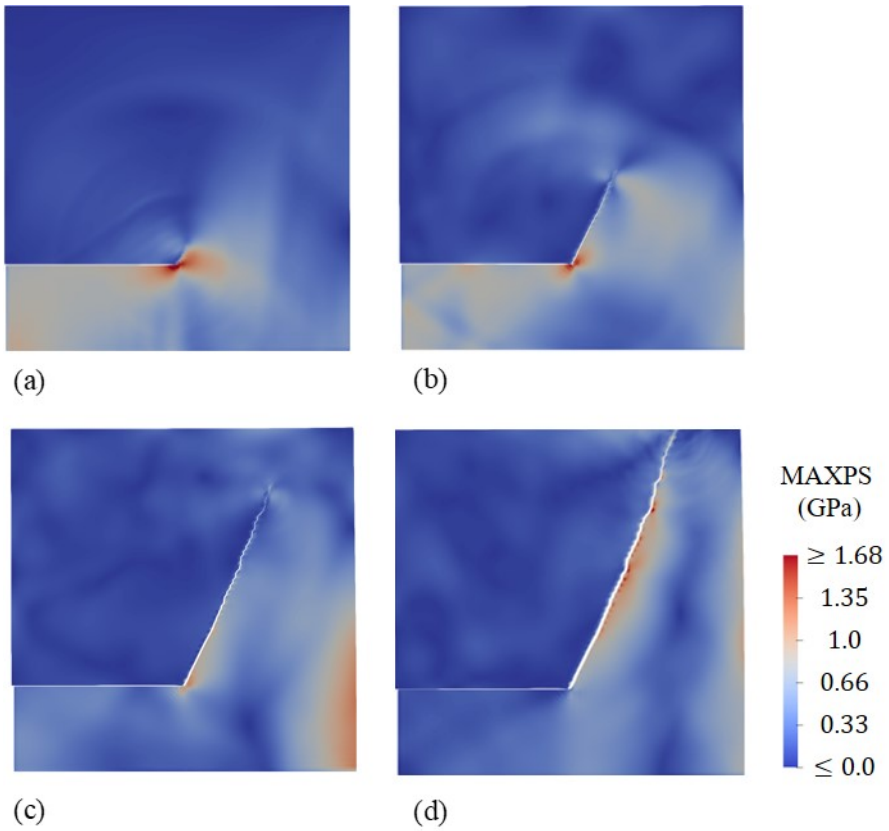

Figure 5.18 The computed crack paths using linear complete formulations on the 120×120 deformed mesh with a maximum principle stress at different time steps: (a) $t = 25.72\,\mu$s; (b) $t = 38.22\,\mu$s; (c) $t = 56.54\,\mu$s; and (d) $t = 78.68\,\mu$s.

at the loading point is applied as a ramp function as

$$V(t) = \begin{cases} V_0 t / t_{\text{ramp}} & t < t_{\text{ramp}} \\ V_0 & t > t_{\text{ramp}} \end{cases} \tag{5.6}$$

where $V_0 = 0.06\,\text{m/s}$ and $t_{\text{ramp}} = 196\,\mu$s. The imposed velocity was calibrated to result in a strain rate of $0.3\,\text{s}^{-1}$ at the midspan which was reported in the experiments (see Reference [36]).

Numerical simulations with three different meshes were carried out: a coarse mesh of around 1000 elements, a medium mesh of around 4000 elements and a fine mesh of around 15000 elements. The finite element meshes are shown in Figures

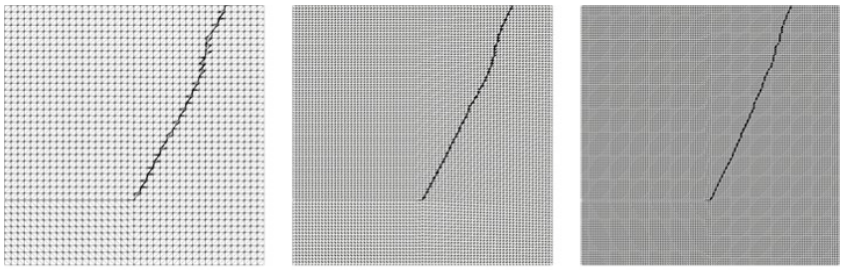

Figure 5.19 Comparison of crack propagation trajectories using linear complete formulation at final simulation step using triangular linear elements (a) 40×40 mesh; (b) 80×80 mesh; and (c) 120×120 mesh.

Table 5.2 Crack propagation angles and timing data using linear complete formulation for the Kalthoff's experiment.

Mesh	Angles(°)		Time(μs)	
	Initial	Overall	Propagation	Simulation
40×40	61.63	64.63	25.55	82.85
80×80	63.02	65.88	22.50	78.43
120×120	65.18	68.77	19.7	77.4

5.21(b)-(d). The numerical experiments were conducted with various offset parameters to capture observed failure patterns. The numerical simulations show that the initial notch location for the transition stage approaches to the experimentally determined value with mesh refinement. As shown in Figures 5.21(b)-(d), the γ_{t} for the fine meshes was obtained as 0.78, which agrees quite well with experimental result of 0.77. The crack propagation paths for each mesh are shown in Figures 5.22-5.24.

The observed three numerical crack patterns for fine mesh are shown in Figure 5.25. As it is shown for $\gamma = 0.75$ the crack propagates only from the offset notch with an angle of 59° which is very similar to the experimental value of 60°. At the final stage of crack growth, the crack rotates a little bit toward the loading point which

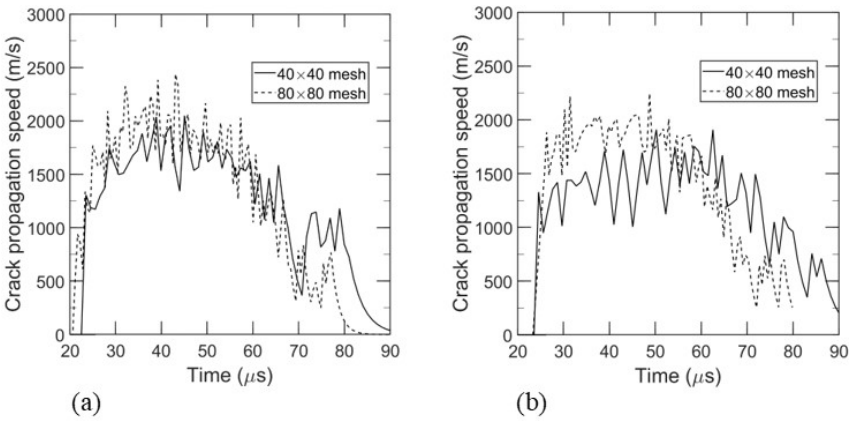

Figure 5.20 Crack speeds for the Kolthoff's experiment simulation: (a) the crack speed of linear complete formulation and (b) the crack speed of the standard XFEM.

was also reported in experiments. For $\gamma = 0.78$ where the offset notch is in transition zone, two cracks are initiated both at the midspan and the notch and propagate simultaneously, but the final failure occurs at the midspan. Finally, for $\gamma = 0.785$, only one main crack is initiated at the midspan and propagates toward the loading point.

5.5 CRACK EXTENSION AND VELOCITY IN THREE-POINT BENDING SPECIMENS

In order to compare the crack speed of the proposed method with those reported in experiments of three-point-bend specimens, we examined an experiment reported by Guo et al. [17]. This experiment has been also numerically modeled by Gonzalo Ruiz et al. [28] in three dimensions. The experimental set-up is shown in Figure 5.26(a). The offset notch is located at 25.4 mm from beam midspan and extended by approximately 13 mm.

The material used in the simulation has the following properties: density $\rho = 2400\text{kg/m}^3$, Young's modulus $E = 32.3\text{GPa}$ and Poisson's ratio $\nu = 0.2$. Since the load-line displacements were measured in experiments, the impact loading can be

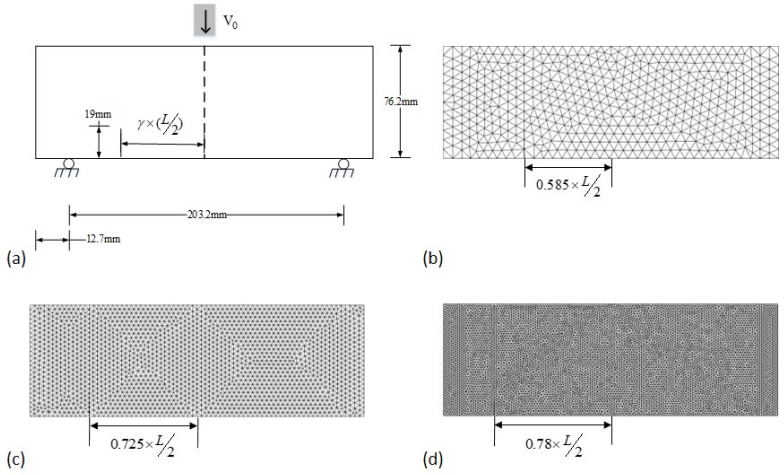

Figure 5.21 The geometry and boundary conditions of three-point-bend specimens and finite element meshes used in numerical simulations for the offset notch at the transition point; (a) experiment set-up; (b) a coarse mesh of around 1000 elements; (c) a medium mesh of around 4000 elements and (d) a fine mesh of around 15000 elements.

applied as a prescribed displacement (for more details, refer to References [28, 17]). The dynamic tensile strength of 7.75MPa (2.5 times of tensile strength) is taken as the maximum tensile stress. A linear cohesive crack model was used with fracture energy of $G_F = 120\text{Jm}^{-2}$. To examine mesh sensitivity, three different triangular meshes were used in the numerical simulations as illustrated in Figures 5.26(b)-(d).

Figure 5.27(a) shows the averaged crack path obtained in experiments. The experiments show that, the crack first grows primarily along an initial angle θ_1 measured from vertical line, then after passing half width of the beam, it rotates θ_2 degrees with respect to initial angle toward the loading point. As shown in Figure 5.27(a), the experimentally computed values of θ_1 and θ_2, are 10° and 16°, respectively. The crack patterns and the crack evolutions for three different meshes are shown in Figure 5.27(b)-(d) and Figures 5.28- 5.30, respectively. The simulation results are listed in

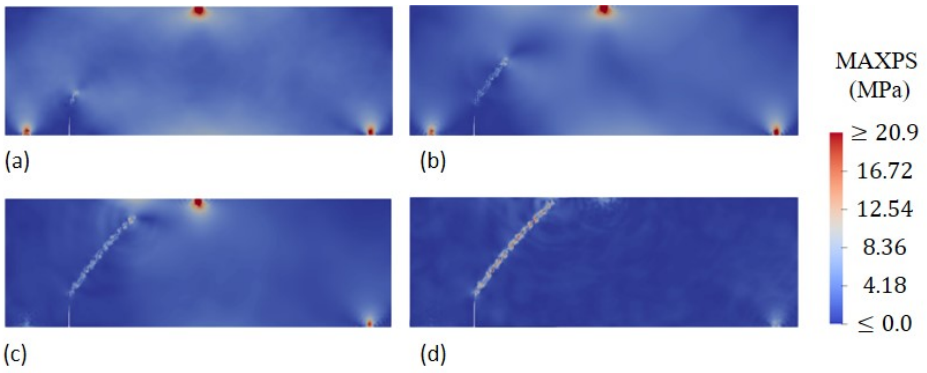

Figure 5.22 The computed crack paths for $\gamma_t = 0.75$ on the fine deformed mesh with a maximum principal stress at different time steps (a) $t = 1142\,\mu$s ; (b) $t = 1180\,\mu$s; (c) $t = 1227\,\mu$s; and (d) $t = 1305\,\mu$s.

Table 5.3. The outcomes show that the crack starts propagating in an earlier time with mesh refinement. All simulations have similar crack propagation paths. In these simulations, the crack propagation angles θ_1 and θ_2 are in excellent agreement with the experimentally observed value of 10° and 16°, respectively.

The crack length history and speed for different meshes are illustrated in

Table 5.3 Crack propagation angles and timing data for the Guo's experiment simulations

Mesh	Angles(°)		Propagation Time (μs)
	Initial(θ_1)	Final(θ_2)	
Coarse mesh	9.5	11.85	360
Medium mesh	9.0	13.1	319
Fine mesh	10.0	14.0	305

Figure 5.31. As it can be seen, the crack speed for the coarse mesh is substantially higher than the experimental speed. For the medium and fine meshes, the crack speeds compare well with observed values. This example demonstrates that in general, the crack speed may not be modeled accurately with very coarse meshes.

Guo's experiment were also solved using linear complete enriched XFEM.

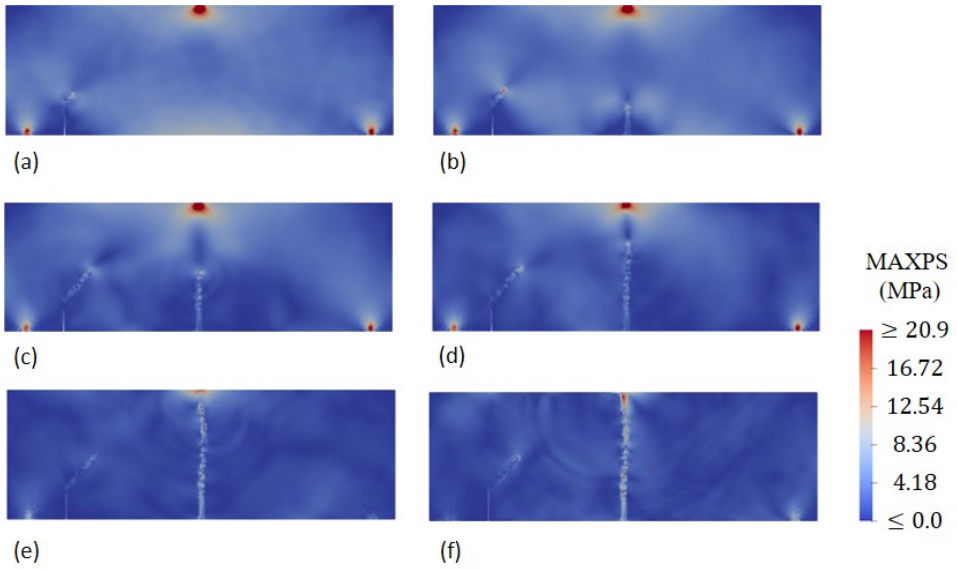

Figure 5.23 The computed crack paths for $\gamma_t = 0.78$ on the fine deformed mesh with a maximum principal stress at different time steps (a) $t = 1329\,\mu$s ; (b) $t = 1350\,\mu$s; (c) $t = 1364\,\mu$s; (d) $t = 1385\,\mu$s; (e) $t = 1423\,$s; and (f) $t = 1456\,\mu$s.

Figures 5.32(b-d) show the crack path obtained in numerical experiments. The crack evolutions for three meshes are shown in Figure 5.33-5.35. The simulation results are also listed in Table 5.4. The results show that the first angle θ_1 has been captured quite accurately with mesh refinement. The second angle θ_2 was obtained slightly less that the experimentally obtained value. These results show that the proposed method can well reproduce the failure in three-pint bend specimens.

The crack length history and speed for different meshes are shown in Figure 5.36. The crack speeds for the linear complete formulation show less mesh dependency than those obtained by previous work depicted in Figure 5.31. However, the crack speed for the coarse is mesh is still higher than the experimental speed. For the medium and fine meshes, the crack speeds compare very well with observed values.

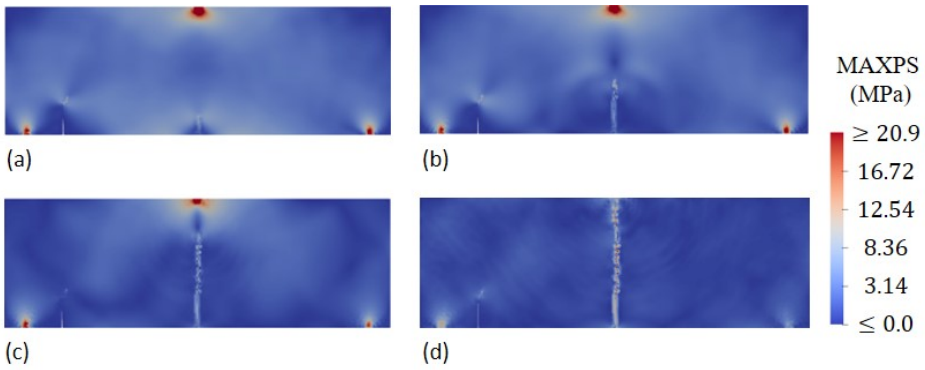

Figure 5.24 The computed crack paths for $\gamma_t = 0.785$ on the fine deformed mesh with a maximum principal stress at different time steps (a) $t = 1316\,\mu$s ; (b) $t = 1330\,\mu$s; (c) $t = 1361\,\mu$s; and (d) $t = 1429\,\mu$s.

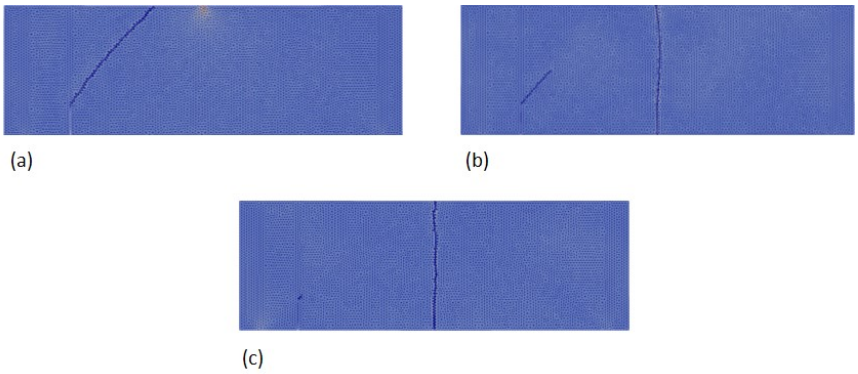

Figure 5.25 Fine mesh crack patterns for different offset parameter γ (a) $\gamma = 0.75$; (b) $\gamma = 0.78$; and (c) $\gamma = 0.785$.

Table 5.4 Crack propagation angles and timing data resulted from linear complete enriched formulation for the Guo's experiment

Mesh	Angles(°)		Propagation Time (μs)
	Initial(θ_1)	Final(θ_2)	
Coarse mesh	14.5	9.0	331.6
Medium mesh	11.5	13.2	309.7
Fine mesh	10.8	12.5	295.4

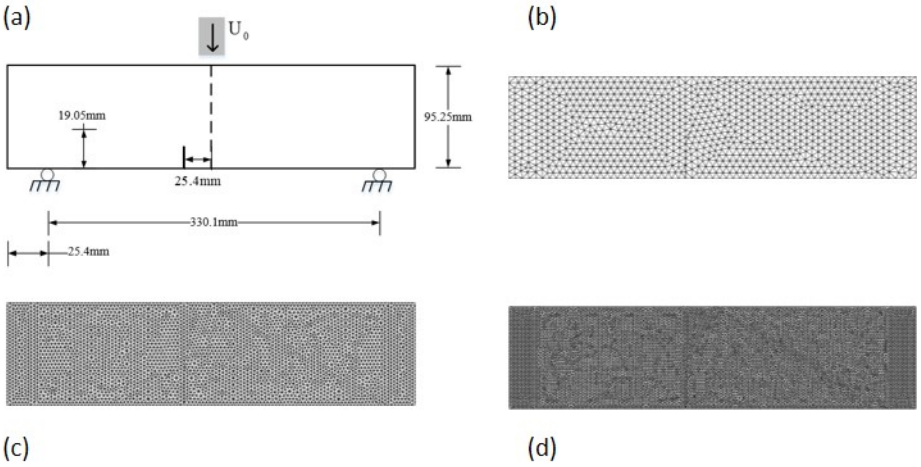

Figure 5.26 The geometry and boundary conditions of Guo's experiment and finite element meshes used in numerical simulations; (a) experiment set-up; (b) a coarse mesh of around 1100 elements; (c) a medium mesh of around 7700 elements and (d) a fine mesh of around 17200 elements.

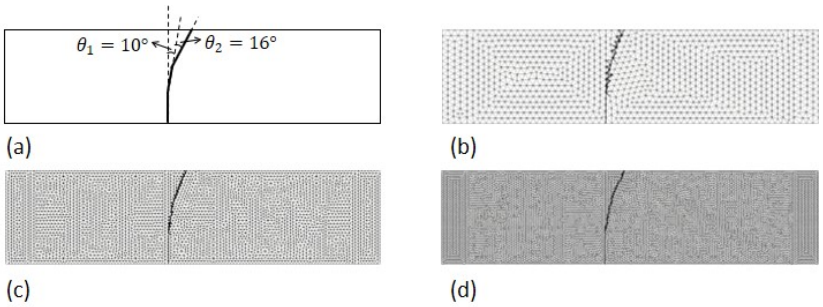

Figure 5.27 The crack patterns for different meshes: (a) coarse mesh (b) medium mesh and (c) fine mesh.

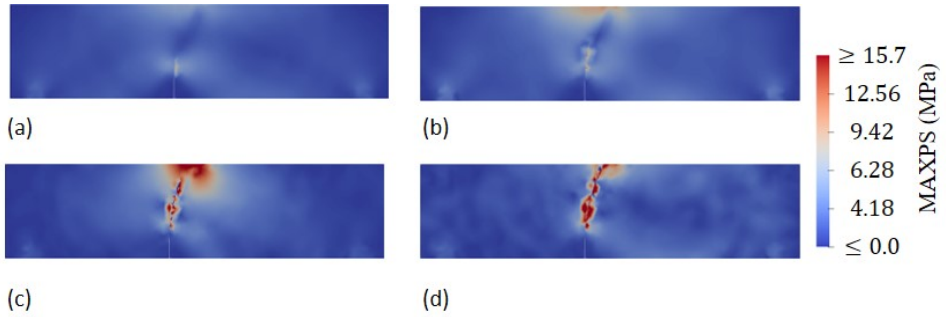

Figure 5.28 The crack evolution for coarse mesh: (a)$t = 369.41\,\mu$s; (b)$t = 486.89\,\mu$s; (c)$t = 606.82\,\mu$s; and (d) $t = 697.72\,\mu$s.

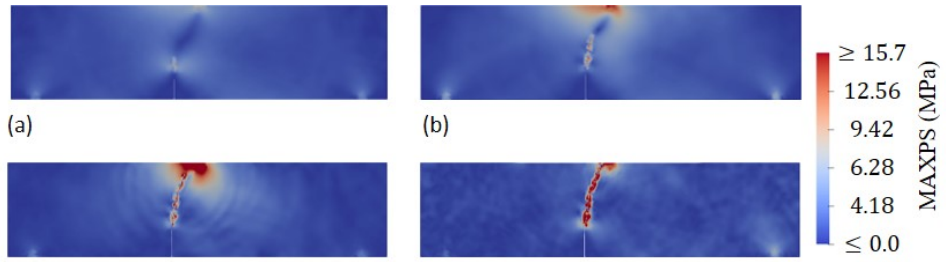

Figure 5.29 The crack evolution for medium mesh: (a)$t = 370.43\,\mu$s; (b)$t = 531.64\,\mu$s; (c)$t = 607.73\,\mu$s; and (d) $t = 742\,\mu$s.

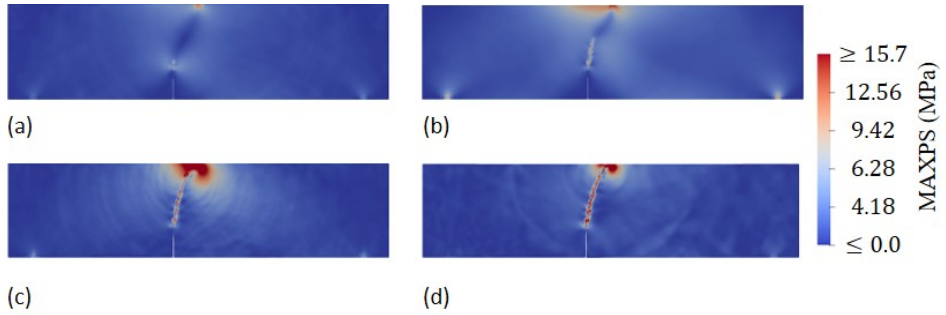

Figure 5.30 The crack evolution for fine mesh: (a)$t = 346.58\,\mu$s; (b)$t = 531\,\mu$s; (c)$t = 616\,\mu$s; and (d) $t = 618\,\mu$s.

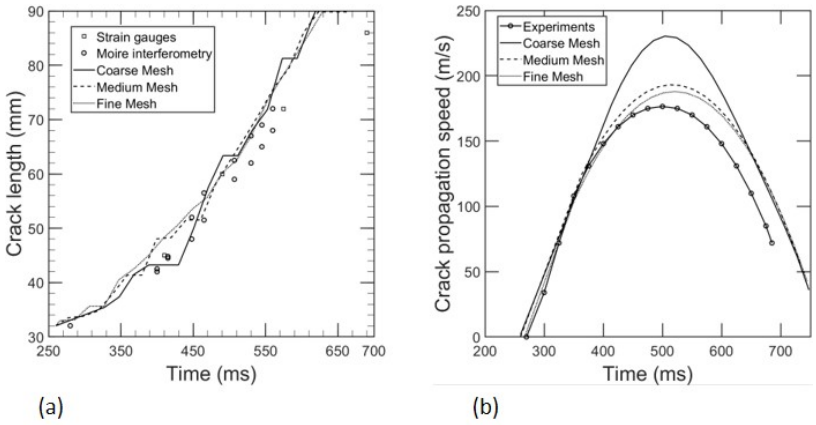

Figure 5.31 Crack length history and crack speeds obtained in numerical simulations for different meshes compared to the Guo's experiment: (a) the crack length histories; and (b) the crack speeds.

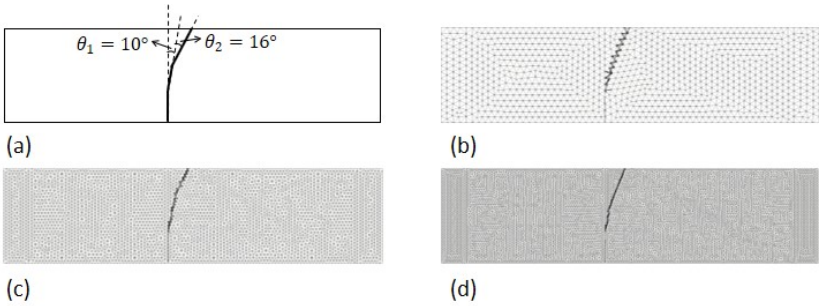

Figure 5.32 The crack patterns using linear complete enriched formulation for different meshes: (a) coarse mesh (b) medium mesh and (c) fine mesh.

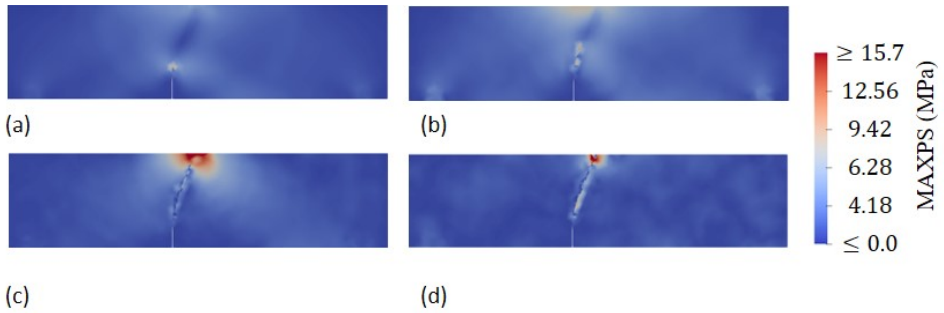

Figure 5.33 The crack evolution resulted from linear complete enriched formulations for coarse mesh: (a)$t = 331.16\,\mu$s; (b)$t = 467.04\,\mu$s; (c)$t = 611.79\,\mu$s; and (d) $t = 785.72\,\mu$s.

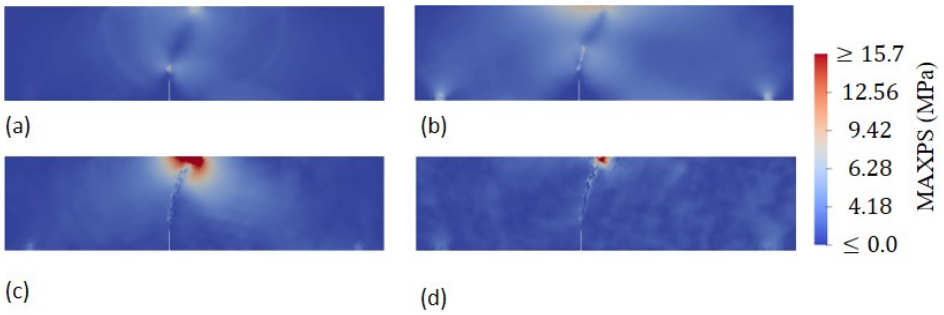

Figure 5.34 The crack evolution resulted from linear complete enriched formulations for medium mesh: (a)$t = 311.36\,\mu$s; (b)$t = 461.87\,\mu$s; (c)$t = 606.87\,\mu$s; and (d) $t = 838.92\,\mu$s.

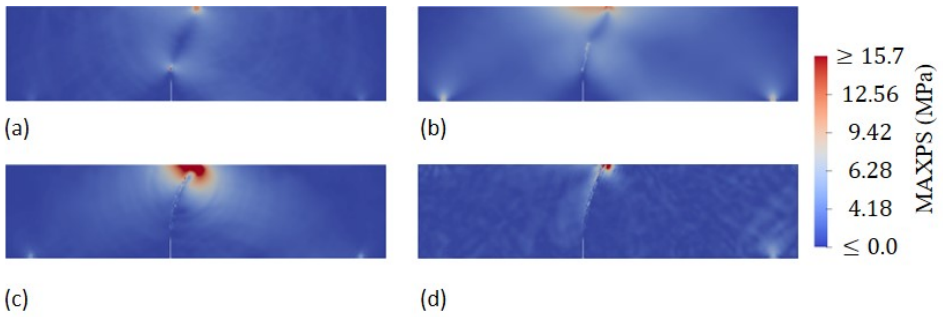

Figure 5.35 The crack evolution resulted from linear complete enriched formulation for fine mesh: (a)$t = 327.57\,\mu$s; (b)$t = 499\,\mu$s; (c)$t = 612.02\,\mu$s; and (d) $t = 773.68\,\mu$s.

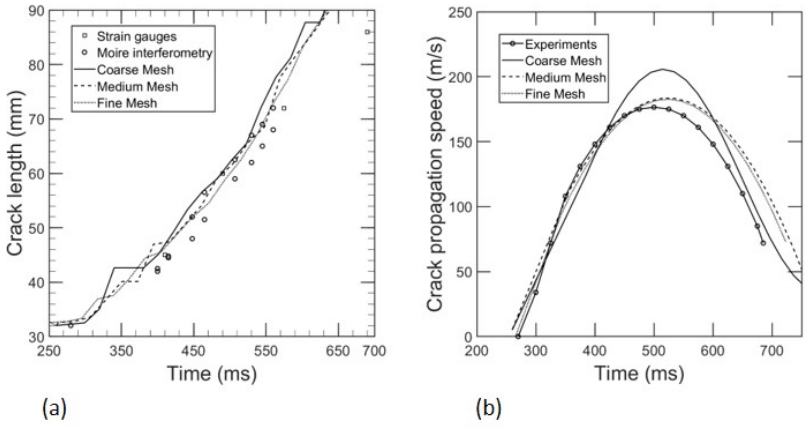

Figure 5.36 Crack length history and crack speeds obtained from linear complete enriched formulation for different meshes compared to the Guo's experiment: (a) the crack length histories; and (b) the crack speeds.

Chapter 6

Conclusion and Future Research

New XFEM-based methods within an explicit time integration scheme have been developed for modeling strong discontinuities in two dimensional planes, which we referred to as non-nodal XFEM methods. In this method, by assigning the enrichment parameters to a set of non-nodal points on the interface and defining their associated enrichment functions such that they satisfy C^0 continuity condition, the discontinuity is modeled within an element without involving element nodes. This feature, in contrast to conventional XFEM, enhances the approximation capabilities to reproduce discontinuous functions and at the same time the polynomial functions required for finite element completeness. Furthermore, excluding the element nodes from construction of enrichment functions dramatically simplifies the XFEM implementation.

A linear complete enriched element within the framework of non-nodal XFEM has been developed for three-node triangular elements. Linear completeness is a crucial criterion for the convergence of finite element methods. In order to reproduce independent linear functions on either side of the interface, a new set of enrichment functions and parameters were introduced for weak discontinuities in a function. Furthermore, a general methodology for constructing the enrichment functions within the framework of non-nodal XFEM for arbitrary discontinuous functions within multi-node elements were introduced.

It was demonstrated through three examples that the proposed method can be successfully used in dynamic crack modeling. In the Kalthoff's experiment, this

method resulted very similar crack patterns independent of the mesh. Furthermore, the crack tip speed discrepancy was negligible with mesh refinement, in contrast to conventional XFEM. For mixed-mode crack propagation in three-point-bend specimens, we analyzed the experiments conducted by John and Shah [18] and Guo et al. [17]. In these sequence of numerical experiments, the overall crack propagation paths agree quite well with those values determined in the experiments. However, the crack propagation angles and the crack tip speeds approached to the experiments by mesh refinement. The numerical examples demonstrate that the method can be used for modeling discontinuities with the added advantage of excluding the element nodes from extended interpolation.

Finally, we would like to point out that the proposed methodology may be used to model different discontinuities and also include higher order polynomials in extended part of interpolation.

The following areas are worthwhile for further study: Menouillard et al. [23] showed that to efficiently solve the system of equations, a lumped mass matrix can be derived by making the kinetic energy for basic motions to be exact. However, their method can be only used for unshifted enrichment functions, which are rarely used in FE programs. Since in the non-nodal XFEM, the enrichment parameters are physically-based quantities, the Menouillard method could potentially be used to introduced a lumped mass matrix.

This dissertation proposed a new XFEM to remove the difficulties arisen by standard XFEM in modeling the strong discontinuities, i.e. cracks. Additional discontinuities could be considered in future models such as crack-tip modeling, weak discontinuities in bi-material elements, strains localizations by shear bands and crack branching. Lastly, the non-nodal XFEM formulation could be further generalized for higher-order elements.

Bibliography

[1] Pedro Areias and Ted Belytschko, *Two-scale shear band evolution by local partition of unity*, International Journal for Numerical Methods in Engineering **66** (2006), no. 5, 878–910.

[2] Ivo Babuška, Uday Banerjee, and John E Osborn, *On principles for the selection of shape functions for the generalized finite element method*, Computer methods in applied mechanics and engineering **191** (2002), no. 49-50, 5595–5629.

[3] Ivo Babuška, Gabriel Caloz, and John E Osborn, *Special finite element methods for a class of second order elliptic problems with rough coefficients*, SIAM Journal on Numerical Analysis **31** (1994), no. 4, 945–981.

[4] Ivo Babuška and Jens M Melenk, *The partition of unity method*, International journal for numerical methods in engineering **40** (1997), no. 4, 727–758.

[5] T Belytschko, D Organ, and C Gerlach, *Element-free galerkin methods for dynamic fracture in concrete*, Computer Methods in Applied Mechanics and Engineering **187** (2000), no. 3-4, 385–399.

[6] T Belytschko and Mazen Tabbara, *Dynamic fracture using element-free galerkin methods*, International Journal for Numerical Methods in Engineering **39** (1996), no. 6, 923–938.

[7] Ted Belytschko and Tom Black, *Elastic crack growth in finite elements with minimal remeshing*, International journal for numerical methods in engineering **45** (1999), no. 5, 601–620.

[8] Ted Belytschko, Hao Chen, Jingxiao Xu, and Goangseup Zi, *Dynamic crack propagation based on loss of hyperbolicity and a new discontinuous enrichment*, International journal for numerical methods in engineering **58** (2003), no. 12, 1873–1905.

[9] Ted Belytschko, Wing Kam Liu, Brian Moran, and Khalil Elkhodary, *Nonlinear finite elements for continua and structures*, John wiley & sons, 2013.

[10] Ted Belytschko, Nicolas Moës, Shuji Usui, and Chandu Parimi, *Arbitrary discontinuities in finite elements*, International Journal for Numerical Methods in Engineering **50** (2001), no. 4, 993–1013.

[11] Jack Chessa, Hongwu Wang, and Ted Belytschko, *On the construction of blending elements for local partition of unity enriched finite elements*, International Journal for Numerical Methods in Engineering **57** (2003), no. 7, 1015–1038.

[12] John Dolbow, Nicolas Moës, and Ted Belytschko, *Discontinuous enrichment in finite elements with a partition of unity method*, Finite elements in analysis and design **36** (2000), no. 3-4, 235–260.

[13] Michael G Duffy, *Quadrature over a pyramid or cube of integrands with a singularity at a vertex*, SIAM journal on Numerical Analysis **19** (1982), no. 6, 1260–1262.

[14] Thomas-Peter Fries, *A corrected xfem approximation without problems in blending elements*, International Journal for Numerical Methods in Engineering **75** (2008), no. 5, 503–532.

[15] Thomas-Peter Fries and Ted Belytschko, *The extended/generalized finite element method: an overview of the method and its applications*, International Journal for Numerical Methods in Engineering **84** (2010), no. 3, 253–304.

[16] Robert Gracie, Jay Oswald, and Ted Belytschko, *On a new extended finite element method for dislocations: core enrichment and nonlinear formulation*, Journal of the Mechanics and Physics of Solids **56** (2008), no. 1, 200–214.

[17] ZK Guo, AS Kobayashi, and NM Hawkins, *Dynamic mixed mode fracture of concrete*, International Journal of Solids and Structures **32** (1995), no. 17-18, 2591–2607.

[18] Reji John and Surendra P Shah, *Mixed-mode fracture of concrete subjected to impact loading*, Journal of Structural Engineering **116** (1990), no. 3, 585–602.

[19] JF Kalthoff and S Winkler, *Failure mode transition at high rates of shear loading*, DGM Informationsgesellschaft mbH, Impact Loading and Dynamic Behavior of Materials **1** (1988), 185–195.

[20] Patrick Laborde, Julien Pommier, Yves Renard, and Michel Salaün, *High-order extended finite element method for cracked domains*, International Journal for Numerical Methods in Engineering **64** (2005), no. 3, 354–381.

[21] W Michael Lai, David H Rubin, Erhard Krempl, and David Rubin, *Introduction to continuum mechanics*, Butterworth-Heinemann, 2009.

[22] Jens M Melenk and Ivo Babuška, *The partition of unity finite element method: basic theory and applications*, Computer methods in applied mechanics and engineering **139** (1996), no. 1-4, 289–314.

[23] Thomas Menouillard, Julien Rethore, Alain Combescure, and Harridh Bung, *Efficient explicit time stepping for the extended finite element method (x-fem)*, International Journal for Numerical Methods in Engineering **68** (2006), no. 9, 911–939.

[24] Nicolas Moës and Ted Belytschko, *Extended finite element method for cohesive crack growth*, Engineering fracture mechanics **69** (2002), no. 7, 813–833.

[25] Nicolas Moës, John Dolbow, and Ted Belytschko, *A finite element method for crack growth without remeshing*, International journal for numerical methods in engineering **46** (1999), no. 1, 131–150.

[26] SE Mousavi and N Sukumar, *Generalized duffy transformation for integrating vertex singularities*, Computational Mechanics **45** (2010), no. 2-3, 127.

[27] Timon Rabczuk, Jeong-Hoon Song, and Ted Belytschko, *Simulations of instability in dynamic fracture by the cracking particles method*, Engineering Fracture Mechanics **76** (2009), no. 6, 730–741.

[28] Gonzalo Ruiz, Anna Pandolfi, and Michael Ortiz, *Three-dimensional cohesive modeling of dynamic mixed-mode fracture*, International Journal for Numerical Methods in Engineering **52** (2001), no. 1-2, 97–120.

[29] A Simone, CA Duarte, and E Van der Giessen, *A generalized finite element method for polycrystals with discontinuous grain boundaries*, International Journal for Numerical Methods in Engineering **67** (2006), no. 8, 1122–1145.

[30] Jeong-Hoon Song, Pedro Areias, and Ted Belytschko, *A method for dynamic crack and shear band propagation with phantom nodes*, International Journal for Numerical Methods in Engineering **67** (2006), no. 6, 868–893.

[31] Natarajan Sukumar, David L Chopp, Nicolas Moës, and Ted Belytschko, *Modeling holes and inclusions by level sets in the extended finite-element method*, Computer methods in applied mechanics and engineering **190** (2001), no. 46-47, 6183–6200.

[32] Giulio Ventura, Robert Gracie, and Ted Belytschko, *Fast integration and weight function blending in the extended finite element method*, International journal for numerical methods in engineering **77** (2009), no. 1, 1–29.

[33] Giulio Ventura, B Moran, and T Belytschko, *Dislocations by partition of unity*, International Journal for Numerical Methods in Engineering **62** (2005), no. 11, 1463–1487.

[34] Giulio Ventura, JX Xu, and T Belytschko, *A vector level set method and new discontinuity approximations for crack growth by efg*, International Journal for numerical methods in engineering **54** (2002), no. 6, 923–944.

[35] Goangseup Zi and Ted Belytschko, *New crack-tip elements for xfem and applications to cohesive cracks*, International Journal for Numerical Methods in Engineering **57** (2003), no. 15, 2221–2240.

[36] Goangseup Zi, Hao Chen, Jingxiao Xu, and Ted Belytschko, *The extended finite element method for dynamic fractures*, Shock and Vibration **12** (2005), no. 1, 9–23.

Appendix A

Reproducing Conditions of Non-Nodal XFEM in Two Dimensions

We want to show that the extended approximation in Equation (2.2) can reproduce the linear fields with identical normal at both sides of the interface as given in the following

$$\begin{aligned} \theta^+(X,Y) &= \alpha_0 + \lambda_1 X + \lambda_2 Y \\ \theta^-(X,Y) &= \beta_0 + \lambda_1 X + \lambda_2 Y \end{aligned} \tag{A.1}$$

where θ is the scalar field with a strong discontinuity along a straight line as demonstrated in Figure 2.2. In Equation (A.1), the identical normal to the fields can be verified as

$$\mathbf{n}^+ = \mathbf{n}^- = \frac{\nabla\theta^+}{\|\nabla\theta^+\|} = \frac{\nabla\theta^-}{\|\nabla\theta^-\|} = \frac{1}{\sqrt{\lambda_1^2+\lambda_2^2}} \begin{bmatrix} \lambda_1 \\ \lambda_2 \end{bmatrix} \tag{A.2}$$

The nodal values for the linear displacement in Equation (A.1) are given by

$$\begin{cases} \theta_1 &= \alpha_0 + \lambda_1 X_1 + \lambda_2 Y_1 \\ \theta_2 &= \beta_0 + \lambda_1 X_2 + \lambda_2 Y_2 \\ \theta_3 &= \beta_0 + \lambda_1 X_3 + \lambda_2 Y_3 \\ [\![\theta]\!]_1 &= \alpha_0 - \beta 0 \\ [\![\theta]\!]_2 &= \alpha_0 - \beta 0 \end{cases} \Rightarrow \begin{bmatrix} \theta_1 \\ \theta_2 \\ \theta_3 \\ [\![\theta]\!]_1 \\ [\![\theta]\!]_2 \end{bmatrix} = \begin{bmatrix} +1 & 0 & X_1 & Y_1 \\ 0 & +1 & X_2 & Y_2 \\ 0 & +1 & X_3 & Y_3 \\ +1 & -1 & 0 & 0 \\ +1 & -1 & 0 & 0 \end{bmatrix} \begin{bmatrix} \alpha_0 \\ \beta_0 \\ \lambda_1 \\ \lambda_2 \end{bmatrix} \tag{A.3}$$

The XFEM approximation can be written in matrix format as follows

$$\begin{bmatrix} \theta^+ \\ \theta^- \end{bmatrix} = \begin{bmatrix} N_1' & N_2' & N_3' & \Psi_1^+ & \Psi_2^+ \\ N_1' & N_2' & N_3' & \Psi_1^- & \Psi_2^- \end{bmatrix} \begin{bmatrix} \theta_1 \\ \theta_2 \\ \theta_3 \\ [\![\theta]\!]_1 \\ [\![\theta]\!]_2 \end{bmatrix} \tag{A.4}$$

Substituting nodal values in Equation (A.3) into Equation (A.4) will result in

$$\begin{aligned} \begin{bmatrix} \theta^+ \\ \theta^- \end{bmatrix} &= \begin{bmatrix} N_1' & N_2' & N_3' & N_4^{4Q} & N_3^{4Q} \\ N_1' & N_2' & N_3' & -N_1^{4Q} & -N_2^{4Q} \end{bmatrix} \begin{bmatrix} +1 & 0 & X_1 & Y_1 \\ 0 & +1 & X_2 & Y_2 \\ 0 & +1 & X_3 & Y_3 \\ +1 & -1 & 0 & 0 \\ +1 & -1 & 0 & 0 \end{bmatrix} \begin{bmatrix} \alpha_0 \\ \beta_0 \\ \lambda_1 \\ \lambda_2 \end{bmatrix} = \\ &= \begin{bmatrix} \sum_{I=1}^{4} N_I^{4Q} & 0 & \sum_{I=1}^{3} N_I' X_I & \sum_{I=1}^{3} N_I' Y_I \\ 0 & \sum_{I=1}^{4} N_I^{4Q} & \sum_{I=1}^{3} N_I' X_I & \sum_{I=1}^{3} N_I' Y_I \end{bmatrix} \begin{bmatrix} \alpha_0 \\ \beta_0 \\ \lambda_1 \\ \lambda_2 \end{bmatrix} = \\ &= \begin{bmatrix} \alpha_0 + \lambda_1 X + \lambda_2 Y \\ \beta_0 + \lambda_1 X + \lambda_2 Y \end{bmatrix} \end{aligned} \tag{A.5}$$

where the second equation is obtained by considering the key equations of the isoparametric shape functions given by $\sum_{I=1}^{4} N_I^{4Q} = 1$, $\sum_{I=1}^{3} N_I' = 1$ and Equation (2.6).

Appendix B

Mapping Among Physical, Parent and Duffy's Coordinates

A triple mapping among physical Cartesian coordinate system, triangular parent domain and Duffy's rectangular parent domain have been illustrated in Figure B.1. Node number 1 plotted in red is considered the node that mapped to an edge in Duffy's domain. Using Mapping 3 which maps the Duffy's rectangular parent coordinates to

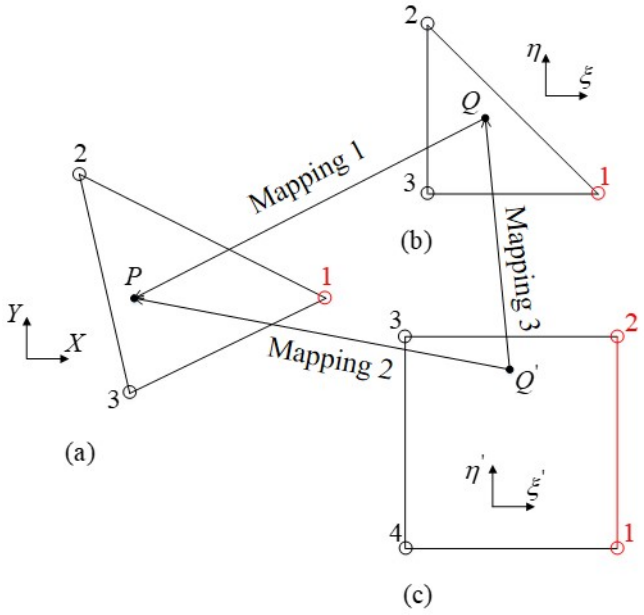

Figure B.1 Mapping among different coordinate systems: (a) physical coordinates; (b) parent coordintes; and (c) Duffy's coordinate.

triangular parent coordinates we can obtain

$$\begin{aligned} \xi &= N_1^{'} \times 1 + N_2^{'} \times 0 + N_3^{'} \times 0 \\ \eta &= N_1^{'} \times 0 + N_2^{'} \times 1 + N_3^{'} \times 0 \end{aligned} \tag{B.1}$$

Using Equation (2.6), Equation (B.1) is rewritten by

$$\begin{aligned} \xi &= 0.5(1 + \xi^{'}) \\ \eta &= 0.25(1 - \xi^{'})(1 + \eta^{'}) \end{aligned} \tag{B.2}$$

Appendix C

Representation of a Crack with Non-Nodal Enrichment Parameters in One Dimension

Considering the displacement jump $[\![u]\!]$ at the point of discontinuity shown in Figure C.1(a) as the enrichment parameter, Equation (2.1) will be rewritten as

$$u(X,t) = \sum_{I=1}^{2} N_I(X)u_I(t) + \Psi(X)[\![u]\!]_{X=X_c} \tag{C.1}$$

Note that since there is only one discontinuity point in one-dimensional crack, the index J has been omitted from enrich part. Substituting the Heaviside step function into Equation (2.17) we will have

$$\begin{aligned} \Psi^+ &= N_1 \\ \Psi^- &= -N_2 \end{aligned} \tag{C.2}$$

This enrichment function is illustrated in Figure C.1(b).

Similar to Appendix A, it can be shown that the interpolation in Equation (C.1) can reproduce a displacement field including two parallel lines on both side of the crack which can be expressed as

$$\begin{aligned} u^+(X) &= \alpha_0 + \lambda X \\ u^-(X) &= \beta_0 + \lambda X \end{aligned} \tag{C.3}$$

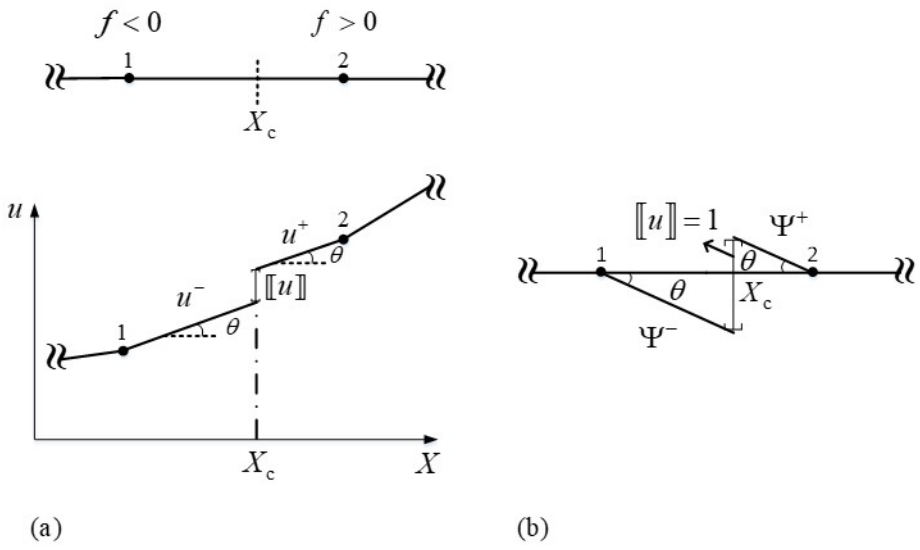

Figure C.1 Strong discontinuity in one dimension: (a) The representation of a discontinuity in a one-dimensional crack model; and (b) One-dimensional crack enrichment function.

Appendix D

REPRODUCING CONDITIONS OF LEANER COMPLETE NON-NODAL XFEM IN ONE DIMENSION

We want to show that the extended approximation in Equation (3.2) can reproduce independent linear fields at both sides of the interface as given in the following

$$\begin{aligned} \theta^{+}(X) &= \alpha_0 + \alpha_1 X \\ \theta^{-}(X) &= \beta_0 + \beta_1 X \end{aligned} \tag{D.1}$$

where θ is the scalar field with strong and weak discontinuities along a straight line as demonstrated in Figure 3.2(a). The nodal values for the linear displacement in Equation (D.1) are given by

$$\begin{cases} \theta_1 & = \beta_0 + \beta_1 X_1 \\ \theta_2 & = \alpha_0 + \alpha_1 X_2 \\ [\![\theta]\!] & = \alpha_0 + \alpha_1 X^{\mathrm{c}} - \beta_0 - \beta_1 X^{\mathrm{c}} \\ [\![L^e \nabla \theta]\!] & = L^e(\alpha_1 - \beta_1) \end{cases} \tag{D.2}$$

The above nodal values can be rearranged in a matrix format as

$$\begin{bmatrix} \theta_1 \\ \theta_2 \\ [\![\theta]\!] \\ [\![L^e \nabla \theta]\!]_1 \end{bmatrix} = \begin{bmatrix} 0 & 0 & 1 & X_1 \\ 0 & X_2 & 0 & 0 \\ 1 & X^{\mathrm{c}} & -1 & -X^{\mathrm{c}} \\ 0 & L^e & 0 & -L^e \end{bmatrix} \begin{bmatrix} \alpha_0 \\ \alpha_1 \\ \beta_0 \\ \beta_1 \end{bmatrix} \tag{D.3}$$

The XFEM approximation can be also written in matrix format as follows

$$\begin{bmatrix} \theta^+ \\ \theta^- \end{bmatrix} = \begin{bmatrix} N_1 & N_2 & N_1 & -sN_1 \\ N_1 & N_2 & -N_2 & -(1-s)N_2 \end{bmatrix} \begin{bmatrix} \theta_1 \\ \theta_2 \\ [\![\theta]\!] \\ [\![L^e \nabla \theta]\!] \end{bmatrix} \tag{D.4}$$

Substituting nodal values in Equation (D.3) into Equation (D.4) will result in

$$\begin{aligned} \begin{bmatrix} \theta^+ \\ \theta^- \end{bmatrix} &= \begin{bmatrix} N_1 & N_2 & N_1 & -sN_1 \\ N_1 & N_2 & -N_2 & -(1-s)N_2 \end{bmatrix} \begin{bmatrix} 0 & 0 & 1 & X_1 \\ 0 & X_2 & 0 & 0 \\ 1 & X^{\mathrm{c}} & -1 & -X^{\mathrm{c}} \\ 0 & L^e & 0 & -L^e \end{bmatrix} \begin{bmatrix} \alpha_0 \\ \alpha_1 \\ \beta_0 \\ \beta_1 \end{bmatrix} = \\ &= \begin{bmatrix} \sum_{I=1}^{2} N_I & \sum_{I=1}^{2} N_I X_I & 0 & 0 \\ 0 & 0 & \sum_{I=1}^{2} N_I & \sum_{I=1}^{2} N_I X_I \end{bmatrix} \begin{bmatrix} \alpha_0 \\ \alpha_1 \\ \beta_0 \\ \beta_1 \end{bmatrix} = \\ &= \begin{bmatrix} \alpha_0 + \alpha_1 X \\ \beta_0 + \beta_1 X \end{bmatrix} \end{aligned} \tag{D.5}$$

where the second equation is obtained by considering the key equations of the isoparametric shape functions given by $\sum_{I=1}^{2} N_I = 1$ and $\sum_{I=1}^{2} N_I X_I = X$

Appendix E

REPRODUCING CONDITIONS OF LINEAR COMPLETE NON-NODAL XFEM IN TWO DIMENSIONS

Let us consider two independent linear fields for the crack position given in Figure 3.4(a) as

$$\begin{aligned} \theta^{+}(X,Y) &= \alpha_0 + \alpha_1 X + \alpha_2 Y \\ \theta^{-}(X,Y) &= \beta_0 + \beta_1 X + \beta_2 Y \end{aligned} \tag{E.1}$$

We want to show that such independent linear functions at both sides of the crack can be reproduced by substituting the nodal and enriched variables in the interpolation given in Equation (3.6). The nodal values for the linear displacement in Equation (E.1) are given by

$$\begin{cases} \theta_1 & = \alpha_0 + \alpha_1 X_1 + \alpha_2 Y_1 \\ \theta_2 & = \alpha_0 + \alpha_1 X_2 + \alpha_2 Y_2 \\ \theta_3 & = \alpha_0 + \alpha_1 X_3 + \alpha_2 Y_3 \\ [\![\theta]\!]_1 = [\![\theta]\!]_{\mathbf{X}=\mathbf{X}_1^{\mathrm{c}}} & = \alpha_0 + \alpha_1 X_1^{\mathrm{c}} + \alpha_2 Y_1^{\mathrm{c}} - \beta_0 - \beta_1 X_1^{\mathrm{c}} - \beta_2 Y_1^{\mathrm{c}} \\ [\![L_1^{\mathrm{c}} \nabla\theta.\mathbf{e}_1^{\mathrm{c}}]\!]_1 = [\![L_1^{\mathrm{c}} \nabla\theta.\mathbf{e}_1^{\mathrm{c}}]\!]_{\mathbf{X}=\mathbf{X}_1^{\mathrm{c}}} & = (\alpha_1 - \beta_1)(X_1^{\mathrm{c}} - X_3^{\mathrm{c}}) + (\alpha_2 - \beta_2)(Y_1^{\mathrm{c}} - Y_3^{\mathrm{c}}) \\ [\![\theta]\!]_2 = [\![\theta]\!]_{\mathbf{X}=\mathbf{X}_2^{\mathrm{c}}} & = \alpha_0 + \alpha_1 X_2^{\mathrm{c}} + \alpha_2 Y_2^{\mathrm{c}} - \beta_0 - \beta_1 X_2^{\mathrm{c}} - \beta_2 Y_2^{\mathrm{c}} \\ [\![L_2^{\mathrm{c}} \nabla\theta.\mathbf{e}_2^{\mathrm{c}}]\!]_2 = [\![L_2^{\mathrm{c}} \nabla\theta.\mathbf{e}_2^{\mathrm{c}}]\!]_{\mathbf{X}=\mathbf{X}_2^{\mathrm{c}}} & = (\alpha_1 - \beta_1)(X_1^{\mathrm{c}} - X_2^{\mathrm{c}}) + (\alpha_2 - \beta_2)(Y_1^{\mathrm{c}} - Y_2^{\mathrm{c}}) \end{cases} \tag{E.2}$$

The above nodal values can be rearranged in a matrix format as

$$\begin{bmatrix} \theta_1 \\ \theta_2 \\ \theta_3 \\ [\![\theta]\!]_1 \\ [\![L_1^{\mathrm{c}} \nabla\theta.\mathbf{e}_1^{\mathrm{c}}]\!]_1 \\ [\![\theta]\!]_2 \\ [\![L_2^{\mathrm{c}} \nabla\theta.\mathbf{e}_2^{\mathrm{c}}]\!]_2 \end{bmatrix} = \begin{bmatrix} 1 & X_1 & Y_1 & 0 & 0 & 0 \\ 0 & 0 & 0 & 1 & X_2 & Y_2 \\ 0 & 0 & 0 & 1 & X_3 & Y_3 \\ 1 & X_1^{\mathrm{c}} & Y_1^{\mathrm{c}} & -1 & -X_1^{\mathrm{c}} & -Y_1^{\mathrm{c}} \\ 0 & X_1^{\mathrm{c}} - X_3^{\mathrm{c}} & Y_1^{\mathrm{c}} - Y_3^{\mathrm{c}} & 0 & -X_1^{\mathrm{c}} + X_3^{\mathrm{c}} & -Y_1^{\mathrm{c}} + Y_3^{\mathrm{c}} \\ 1 & X_2^{\mathrm{c}} & Y_2^{\mathrm{c}} & -1 & -X_2^{\mathrm{c}} & -Y_2^{\mathrm{c}} \\ 0 & X_1^{\mathrm{c}} - X_2^{\mathrm{c}} & Y_1^{\mathrm{c}} - Y_2^{\mathrm{c}} & 0 & -X_1^{\mathrm{c}} + X_2^{\mathrm{c}} & -Y_1^{\mathrm{c}} + Y_2^{\mathrm{c}} \end{bmatrix} \begin{bmatrix} \alpha_0 \\ \alpha_1 \\ \alpha_2 \\ \beta_0 \\ \beta_1 \\ \beta_2 \end{bmatrix} \tag{E.3}$$

where we have used

$$\mathbf{e}_1^{\mathrm{c}} = \frac{1}{L_1^{\mathrm{c}}} \begin{bmatrix} X_1 - X_3 \\ Y_1 - Y_3 \end{bmatrix} \quad \mathbf{e}_2^{\mathrm{c}} = \frac{1}{L_2^{\mathrm{c}}} \begin{bmatrix} X_1 - X_2 \\ Y_1 - Y_2 \end{bmatrix} \tag{E.4}$$

The XFEM approximation can be written in matrix format as follows

$$\begin{bmatrix} \theta^+ \\ \theta^- \end{bmatrix} = \begin{bmatrix} N_1' & N_2' & N_3' & \Psi_1^{\mathrm{u}+} & \Psi_1^{\nabla\mathrm{u}+} & \Psi_2^{\mathrm{u}+} & \Psi_2^{\nabla\mathrm{u}+} \\ N_1' & N_2' & N_3' & \Psi_1^{\mathrm{u}-} & \Psi_1^{\nabla\mathrm{u}-} & \Psi_2^{\mathrm{u}-} & \Psi_2^{\nabla\mathrm{u}-} \end{bmatrix} \begin{bmatrix} \theta_1 \\ \theta_2 \\ \theta_3 \\ [\![\theta]\!]_1 \\ [\![L_1^{\mathrm{c}} \nabla\theta.\mathbf{e}_1^{\mathrm{c}}]\!]_1 \\ [\![\theta]\!]_2 \\ [\![L_2^{\mathrm{c}} \nabla\theta.\mathbf{e}_2^{\mathrm{c}}]\!]_2 \end{bmatrix} \tag{E.5}$$

Substituting the unknowns in Equation (E.3) into Equation (E.5) will result in

$$
\begin{aligned}
\begin{bmatrix} \theta^{+} \\ \theta^{-} \end{bmatrix} &= \begin{bmatrix} N_1' & N_2' & N_3' & \Psi_1^{\mathrm{u}+} & \Psi_1^{\nabla \mathrm{u}+} & \Psi_2^{\mathrm{u}+} & \Psi_2^{\nabla \mathrm{u}+} \\ N_1' & N_2' & N_3' & \Psi_1^{\mathrm{u}-} & \Psi_1^{\nabla \mathrm{u}-} & \Psi_2^{\mathrm{u}-} & \Psi_2^{\nabla \mathrm{u}-} \end{bmatrix} \times \\
&\begin{bmatrix} 1 & X_1 & Y_1 & 0 & 0 & 0 \\ 0 & 0 & 0 & 1 & X_2 & Y_2 \\ 0 & 0 & 0 & 1 & X_3 & Y_3 \\ 1 & X_1^{\mathrm{c}} & Y_1^{\mathrm{c}} & -1 & -X_1^{\mathrm{c}} & -Y_1^{\mathrm{c}} \\ 0 & X_1^{\mathrm{c}} - X_3^{\mathrm{c}} & Y_1^{\mathrm{c}} - Y_3^{\mathrm{c}} & 0 & -X_1^{\mathrm{c}} + X_3^{\mathrm{c}} & -Y_1^{\mathrm{c}} + Y_3^{\mathrm{c}} \\ 1 & X_2^{\mathrm{c}} & Y_2^{\mathrm{c}} & -1 & -X_2^{\mathrm{c}} & -Y_2^{\mathrm{c}} \\ 0 & X_1^{\mathrm{c}} - X_2^{\mathrm{c}} & Y_1^{\mathrm{c}} - Y_2^{\mathrm{c}} & 0 & -X_1^{\mathrm{c}} + X_2^{\mathrm{c}} & -Y_1^{\mathrm{c}} + Y_2^{\mathrm{c}} \end{bmatrix} \begin{bmatrix} \alpha_0 \\ \alpha_1 \\ \alpha_2 \\ \beta_0 \\ \beta_1 \\ \beta_2 \end{bmatrix} = \\
&= \sum_{I=1}^{3} N_I' \begin{bmatrix} 1 & X_I & Y_I & 0 & 0 & 0 \\ 0 & 0 & 0 & 1 & X_I & Y_I \end{bmatrix} \begin{bmatrix} \alpha_0 \\ \alpha_1 \\ \alpha_2 \\ \beta_0 \\ \beta_1 \\ \beta_2 \end{bmatrix} = \\
&= \begin{bmatrix} \alpha_0 + \alpha_1 X + \alpha_2 Y \\ \beta_0 + \beta_1 X + \beta_2 Y \end{bmatrix}
\end{aligned}
\tag{E.6}
$$

where we have used the key equations of the isoparametric shape functions. Furthermore, we have extensively used the side-splitter theorem to substitute the parameters s_1 and s_2. Figure E.1 illustrates two different triangles for the computation of s_1 that leads to two different equations.

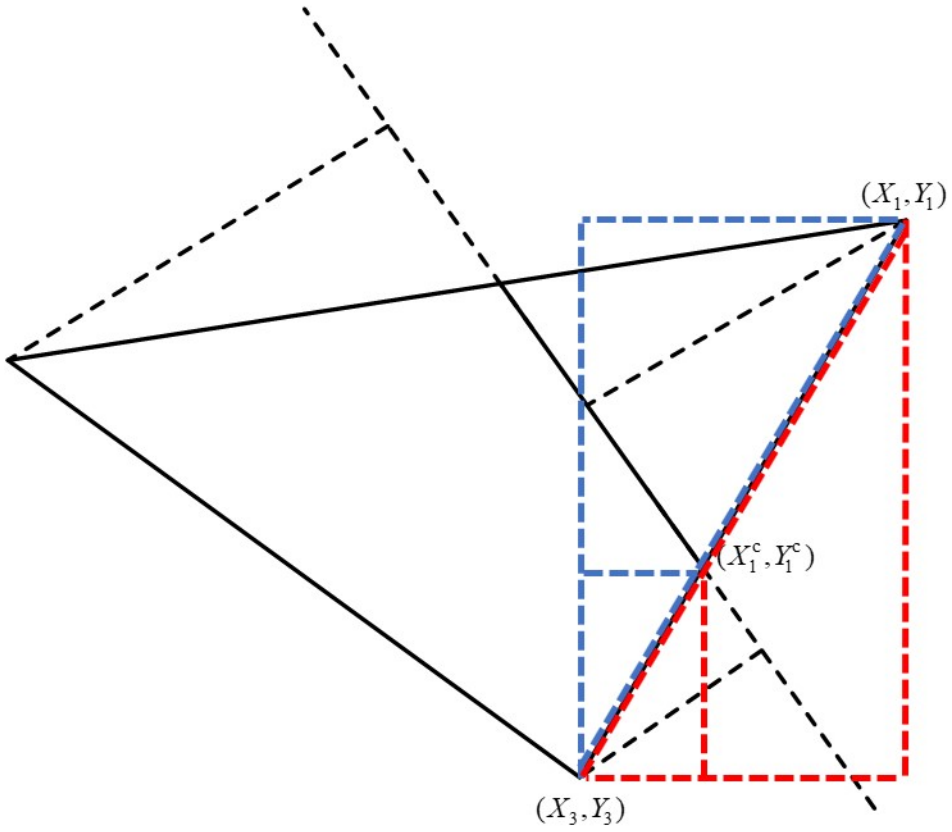

Figure E.1 Application of side-splitter theorem for the computations of s_1; the red triangle gives $s_1 = (Y_1^c - Y_3)/(Y_1 - Y_3)$ and the blue triangle gives $s_1 = (X_1^c - X_3)/(X_1 - X_3)$.